REPORT DOCUMENTATION PAGE

Form Approved OMB NO. 0704-0188

1. REPORT DATE (DD-MM-YYYY) 20-01-2014	2. REPORT TYPE Final Report	3. DATES COVERED (From - To) 1-Nov-2008 - 31-Oct-2013

4. TITLE AND SUBTITLE
A Study of Supersonic Compression-Corner Interactions using Hybrid LES/RANS Models

5a. CONTRACT NUMBER
W911NF-08-1-0430

5b. GRANT NUMBER

5c. PROGRAM ELEMENT NUMBER
611102

6. AUTHORS
Jack R. Edwards

5d. PROJECT NUMBER

5e. TASK NUMBER

5f. WORK UNIT NUMBER

7. PERFORMING ORGANIZATION NAMES AND ADDRESSES
North Carolina State University
Research Administration
2701 Sullivan Drive, Suite 240
Raleigh, NC 27695 -7514

8. PERFORMING ORGANIZATION REPORT NUMBER

9. SPONSORING/MONITORING AGENCY NAME(S) AND ADDRESS (ES)
U.S. Army Research Office
P.O. Box 12211
Research Triangle Park, NC 27709-2211

10. SPONSOR/MONITOR'S ACRONYM(S)
ARO

11. SPONSOR/MONITOR'S REPORT NUMBER(S)
54033-EG.11

12. DISTRIBUTION AVAILIBILITY STATEMENT
Approved for Public Release; Distribution Unlimited

13. SUPPLEMENTARY NOTES
The views, opinions and/or findings contained in this report are those of the author(s) and should not contrued as an official Department of the Army position, policy or decision, unless so designated by other documentation.

14. ABSTRACT

This research has developed a new hybrid large-eddy /Reynolds-averaged Navier-Stokes turbulence closure strategy specifically designed for strongly interacting, wall-bounded flows. The model differs from its predecessor in that the need to pre-calibrate a model constant is removed through the use of ensemble-averaged turbulence information to estimate an outer-layer turbulence length scale. The model has been applied to a variety of shock / boundary layer
interactions and has shown a good level of predictive capability for both mean and second-moment quantities. A

15. SUBJECT TERMS
large-eddy simulation, shock-boundary layer interactions

16. SECURITY CLASSIFICATION OF:			17. LIMITATION OF ABSTRACT	15. NUMBER OF PAGES	19a. NAME OF RESPONSIBLE PERSON Jack Edwards
a. REPORT UU	b. ABSTRACT UU	c. THIS PAGE UU	UU		19b. TELEPHONE NUMBER 919-515-5264

Standard Form 298 (Rev 8/98)
Prescribed by ANSI Std. Z39.18

Report Title

A Study of Supersonic Compression-Corner Interactions using Hybrid LES/RANS Models

ABSTRACT

This research has developed a new hybrid large-eddy /Reynolds-averaged Navier-Stokes turbulence closure strategy specifically designed for strongly interacting, wall-bounded flows. The model differs from its predecessor in that the need to pre-calibrate a model constant is removed through the use of ensemble-averaged turbulence information to estimate an outer-layer turbulence length scale. The model has been applied to a variety of shock / boundary layer

interactions and has shown a good level of predictive capability for both mean and second-moment quantities. A specific result of the shock / boundary layer interaction study is a strong correlation between the most probable time of a fluid within the recirculation region formed through shock interaction and the dominant low-frequency signal of the interaction. This provides evidence that the appearance of a low-frequency mode of separation-shock unsteadiness is intimately connected with the structure of the backflow region and the mean entrainment patterns. With this knowledge in place, it may be possible to predict low-frequency dynamics of complicated interactions by examination of the mean structure of the interactions. The LES/RANS model was also tested for turbulent flow over an airfoil near static stall as an initial step toward its use in predicting dynamic stall

---

Enter List of papers submitted or published that acknowledge ARO support from the start of the project to the date of this printing. List the papers, including journal references, in the following categories:

(a) Papers published in peer-reviewed journals (N/A for none)

Received Paper

TOTAL:

Number of Papers published in peer-reviewed journals:

(b) Papers published in non-peer-reviewed journals (N/A for none)

Received Paper

TOTAL:

Number of Papers published in non peer-reviewed journals:

(c) Presentations

Number of Presentations: 0.00

Non Peer-Reviewed Conference Proceeding publications (other than abstracts):

Received	Paper

TOTAL:

Number of Non Peer-Reviewed Conference Proceeding publications (other than abstracts):

Peer-Reviewed Conference Proceeding publications (other than abstracts):

Received		Paper
08/28/2013	10.00	Jianghua Ke, Jack Edwards. RANS and LES/RANS Simulation of Airfoils under Static and Dynamic Stall, 51st AIAA Aerospace Sciences Meeting including the New Horizons Forum and Aerospace Exposition. 05-JAN-13, Grapevine (Dallas/Ft. Worth Region), Texas. : ,
08/30/2012	5.00	Daniel Gieseking, Jack Edwards, Jung-Il Choi. Simulation of a Mach 3 24-degree Compression-Corner Interaction using LES/RANS Models, 2011 Joint Propulsion Conference. 01-AUG-11, . : ,

TOTAL: **2**

Number of Peer-Reviewed Conference Proceeding publications (other than abstracts):

(d) Manuscripts

Received		Paper
01/14/2011	3.00	Daniel A. Gieseking, Jack R. Edwards. Simulations of a Mach 3 Compression Corner Interaction using LES/RANS Models, 49th AIAA Aerospace Sciences Meeting, Orlando, FL January, 2011 (01 2011)
05/20/2011	4.00	Daniel A. Gieseking, Jung-Il Choi, Jack R. Edwards, Hassan A. Hassan. Compressible Flow Simulations Using a New LES/RANS Model, AIAA Journal (05 2011)
08/30/2012	8.00	Daniel Gieseking, Jung-Il Choi, Jack Edwards, Hassan Hassan. Compressible-Flow Simulations using a New Large-Eddy Simulation / Reynolds-averaged Navier-Stokes Model, AIAA Journal (10 2011)
08/30/2012	9.00	Daniel Gieseking, Jack Edwards. Simulations of a Mach 3 Compression Ramp Interaction using Large-Eddy Simulation/ Reynolds-averaged Navier-Stokes Models, AIAA Journal (01 2012)
TOTAL:		**4**

Number of Manuscripts:

Books

Received	Paper
TOTAL:	

Patents Submitted

Patents Awarded

Awards

Graduate Students

NAME	PERCENT_SUPPORTED	Discipline
Daniel A. Gieseking	0.50	
Ilya Zilberter	0.50	
Jianghua Ke	0.50	
FTE Equivalent:	**1.50**	
Total Number:	**3**	

Names of Post Doctorates

NAME	PERCENT_SUPPORTED
FTE Equivalent:	
Total Number:	

Names of Faculty Supported

NAME	PERCENT_SUPPORTED	National Academy Member
Jack R. Edwards	0.11	
FTE Equivalent:	**0.11**	
Total Number:	**1**	

Names of Under Graduate students supported

NAME	PERCENT_SUPPORTED
FTE Equivalent:	
Total Number:	

Student Metrics

This section only applies to graduating undergraduates supported by this agreement in this reporting period

The number of undergraduates funded by this agreement who graduated during this period: 0.00

The number of undergraduates funded by this agreement who graduated during this period with a degree in science, mathematics, engineering, or technology fields:...... 0.00

The number of undergraduates funded by your agreement who graduated during this period and will continue to pursue a graduate or Ph.D. degree in science, mathematics, engineering, or technology fields:...... 0.00

Number of graduating undergraduates who achieved a 3.5 GPA to 4.0 (4.0 max scale):...... 0.00

Number of graduating undergraduates funded by a DoD funded Center of Excellence grant for Education, Research and Engineering:...... 0.00

The number of undergraduates funded by your agreement who graduated during this period and intend to work for the Department of Defense 0.00

The number of undergraduates funded by your agreement who graduated during this period and will receive scholarships or fellowships for further studies in science, mathematics, engineering or technology fields:...... 0.00

Names of Personnel receiving masters degrees

NAME	
Daniel Gieseking	
Total Number:	**1**

Names of personnel receiving PHDs

NAME

Total Number:

Names of other research staff

NAME	PERCENT_SUPPORTED

FTE Equivalent:
Total Number:

Sub Contractors (DD882)

Inventions (DD882)

Scientific Progress

Technology Transfer

A Study of Supersonic Compression-Corner Interactions using Hybrid LES/RANS Models

Final Technical Report

Army Research Office
W911NF-08-1-0430
Submitted by

Dr. Jack R. Edwards
Department of Mechanical and Aerospace Engineering
Campus Box 7910
North Carolina State University
Raleigh, NC 27695

To

Department of the Army
U.S. Army Research, Development and Engineering Command Acquisition Center
(Attn. Dr. Frederick Ferguson, ARO Grants Representative)
Research Triangle Park Contracting Division
P.O. Box 12211
Research Triangle Park, North Carolina, 27709-2211

Table of Contents

Project Abstract (Original Proposal)

Many experimental investigations have noted that complex shock / boundary layer interactions exhibit large-scale, low frequency motion that is distinct from that associated from wall-layer turbulence. This motion results in fluctuating pressure and heat-transfer loads that can adversely affect the performance of supersonic missile systems, among others. Accurate predictions of such effects would appear to require a time-dependent modeling strategy, such as large-eddy simulation (LES) or direct numerical simulation (DNS). The application of these techniques to flows at practical Reynolds numbers requires immense computational resources, and as yet, very few studies have provided one-to-one comparisons with experimental data. A promising alternative to traditional LES/DNS are hybrid large-eddy / Reynolds-averaged Navier-Stokes (LES/RANS) models, which essentially function as a large-eddy simulation away from solid surfaces but revert to a RANS-based closure near solid surfaces. Recent simulations of two- and three-dimensional shock / boundary layer interactions using a class of "zonal" LES/RANS methods developed at North Carolina State University have shown that these techniques can predict time-averaged flow field properties as well as or better than RANS models. The techniques naturally capture both large-scale and small-scale flow features, but an open question is whether the dynamics of the shock / boundary layer interactions is predicted correctly. This tightly focused research effort will attempt to answer this question by conducting detailed hybrid LES/RANS simulations of the Mach 5, 28 degree compression-corner flows studied by David Dolling's group at the University of Texas. This data is the most comprehensive set available for studying shock interaction dynamics and includes conditionally-averaged pitot and static pressure distributions, wavelength, amplitude, and frequency information associated with the shock structure, and cross-correlation analyses. Simulations will be conducted for this interaction and will involve investigation of the effects of variations in the turbulence modeling parameters, the extent of the computational domain, and the degree of mesh refinement on the predictions. Data extraction will mimic that used in the experimental measurements (to the extent possible). This will enable the one-to-one, time-resolved comparisons necessary for a complete assessment. Results obtained through a successful validation should provide directions for improvement in less-expensive, lower-fidelity models (unsteady RANS or very large eddy simulation (VLES)) and will perhaps yield new insights into the causes of large-scale unsteadiness in flows driven by shock / boundary layer interactions.

1. Overview

This project has resulted in the development of a new hybrid large-eddy / Reynolds-averaged Navier-Stokes (LES/RANS) simulation strategy that models near-wall turbulence through unsteady RANS concepts. A flow-dependent blending function, dependent on both instantaneous and ensemble-averaged turbulence quantities, is used to facilitate the RANS to LES transition, and in contrast to other methods of this type (e.g. Detached Eddy Simulation), the transition is not directly dependent on the mesh spacing. In contrast to our earlier ARO-sponsored work in this scope, the new methodology does not require the specification of a model calibration constant. Rather, the use of both ensemble-averaged and instantaneous data enables the model to self-adjust to changes in the turbulence length scales – a feature not found in other strategies. The model has been developed specifically for high-speed flow applications and has been extensively tested for shock / boundary layer interactions as well as scramjet combustor flowfields. The model has also been used to predict turbulent flow over airfoils near static stall. A supplement to this project, awarded in 2010, focused on the development of data-mining strategies based on LES/RANS results and on the use of 'pure' (non-hybridized) large-eddy simulations as a way of identifying weaknesses in the LES/RANS closure assumptions, specifically within the 'transition region' where the model shifts from (unsteady) RANS to LES.

This report is organized as follows. Section 2 presents details of the new model, including the rationale behind its development as well as recent modifications designed to improve its performance in certain situations. Sections 3-8 describe several validation studies, ranging from boundary layer simulations to fully 3D shock / boundary layer interactions to turbulent flow over an airfoil near static stall. Section 9 discusses the results of several wall-resolved large-eddy simulations designed to provide data to improve the LES/RANS model, and Section 10 discusses the use of LES/RANS data to evaluate RANS models for shock / boundary layer interactions. A summary of the project is presented in Section 11. Publications, students supported, technology transfer activities, and other connections are presented as the last part of this report.

2. Model Development

To anchor the description of the new model, a brief development of the original NCSU LES/RANS model [1,2], developed under prior ARO support, is presented first. The original model was applied to a variety of flows [3-5] with good success, yet its need for a calibration step to pre-select a model constant reduces its generality.

2.1. Original LES/RANS model description

In contrast to detached eddy simulation (DES) and related strategies, the original approach is designed to transition from RANS to LES deep within the boundary layer, at approximately the location where the boundary layer shifts from logarithmic to wake-like behavior. Menter's k-ω model, summarized in brief below, is used as the basis.

$$\frac{\partial(\rho k)}{\partial t}+\frac{\partial(\rho k u_j)}{\partial x_j}=\mu_t S^2-\beta^*\rho\omega k+\frac{\partial}{\partial x_j}\left[(\mu+\sigma_k\mu_t)\frac{\partial k}{\partial x_j}\right] \tag{2.1.1}$$

$$\frac{\partial(\rho\omega)}{\partial t} + \frac{\partial(\rho\omega u_j)}{\partial x_j} = \gamma\rho S^2 - \beta\rho\omega^2 + \frac{\partial}{\partial x_j}\left[(\mu + \sigma_\omega \mu_t)\frac{\partial \omega}{\partial x_j}\right] + 2(1 - F_1)\rho\sigma_{\omega 2}\frac{1}{\omega}\frac{\partial k}{\partial x_j}\frac{\partial \omega}{\partial x_j} \qquad (2.1.2)$$

where S is defined as the magnitude of the vorticity vector for the cases presented in this report. Hybridization of the above equation is accomplished simply by re-defining the eddy viscosity:

$$\mu_t = \rho[\Gamma\frac{k}{\omega} + (1-\Gamma)\nu_{t,sgs}], \qquad (2.1.3)$$

with the subgrid viscosity specified as

$$\nu_{t,sgs} = C_M S^{1/2}(q^2)^{1/4}\Delta^{3/2}, C_M = 0.06 \qquad (2.1.4)$$

An estimate of the subgrid kinetic energy is obtained by test-filtering the resolved-scale velocity data:

$$q^2 = \frac{1}{2}(\tilde{u}_k - \hat{\tilde{u}}_k)^2 \qquad (2.1.5)$$

The response of the model is dictated by the blending function Γ, a time-dependent quantity that reaches a value of unity where an unsteady RANS response is desired and zero where an LES response is desired. It should be mentioned that, because of the effect of unsteady strain rates in enhancing the production of k and ω, one cannot expect that the ensemble-averaged values of k and ω will be equivalent to those obtained under steady-state assumptions (even with Γ equal to 1). In fact, the production of k is greatly enhanced by unsteady strain rates; the production of ω less so.

The blending function used in Refs. [1] and [2] is based on the ratio of the wall distance d to a modeled form of the Taylor micro-scale:

$$\Gamma = \frac{1}{2}\left(1 - \tanh[5(\frac{\kappa}{\sqrt{C_\mu}}\eta^2 - 1) - \phi]\right), \qquad (2.1.6)$$

$$\eta = \frac{d}{\alpha_1 \lambda_T} \qquad (2.1.7)$$

where the Taylor micro-scale is defined as

$$\lambda_T = \sqrt{\nu / C_\mu \omega} \qquad (2.1.8)$$

The constant $\phi = \tanh^{-1}(0.98)$ shifts the balancing position (where $\frac{\kappa}{\sqrt{C_\mu}}\eta^2 = 1$) from Γ=0.5 to Γ = 0.99. It should be mentioned that the shifting parameter ϕ actually corrects for the fact that the time-averaged value for ω is larger than the RANS value because of the enhancement of turbulence production mentioned above.

The constant α_1 is chosen to force the average LES to RANS transition position (Γ= 0.99) for equilibrium boundary layers to occur at the point where the wake law starts to deviate from the log law. To determine α_1 for a particular inflow boundary layer, the following method is used. First, a prediction of the equilibrium boundary layer is obtained (given free-stream properties, a specified wall thermal condition, and a value for the boundary layer thickness) from Coles' Law of the Wall / Wake along with the Van Driest transformation. An initial estimate for the outer extent of the log layer is defined by finding the value of d_w^+ such that

$$\left(\frac{1}{\kappa}\ln(d_w^+)+C\right)/\left(\frac{u_{vd}}{u_\tau}\right)=0.98 \tag{2.1.9}$$

The value of $d^+ = u_\tau d/\nu$ that corresponds to this value of d_w^+ is then found through the use of Walz's formula for the static temperature distribution within the boundary layer:

$$\frac{T}{T_\infty}=\frac{T_w}{T_\infty}+\frac{(T_{aw}-T_w)}{T_\infty}\frac{u}{u_\infty}-r\frac{(\gamma-1)}{2}M_\infty^2\left(\frac{u}{u_\infty}\right)^2 \tag{2.1.10}$$

The model constant is then found by the equivalence $d^+ = \alpha_1{}^2$, which arises from the use of inner-layer scaling arguments for k and ω. Specifically, in the logarithmic region, one has $\omega = u_\tau/(\kappa d\sqrt{C_\mu})$, where κ is the Von Karman constant, $C_\mu = \beta^* = 0.09$, and u_τ is the friction velocity. Substituting this into Eq. 2.1.8 and Eq. 2.17 in succession, one finds that

$$\frac{\kappa}{\sqrt{C_\mu}}\eta^2=\frac{\kappa}{\sqrt{C_\mu}}\frac{C_\mu d^2\omega}{\alpha_1^2\nu}=\frac{u_\tau d}{\alpha_1^2\nu}=\frac{d^+}{\alpha_1^2}=1 \tag{2.1.11}$$

at the balancing position. Figure 2.1.1 shows an example of the positioning of the blending function within a compressible boundary layer. This procedure requires free-stream information and a target boundary layer thickness, both of which are specific to a particular boundary layer. As such, the calibration procedure is not universal and the constant that results must be adjusted on a case-by-case basis. Nevertheless, Ref. [2] in particular shows that the model as described

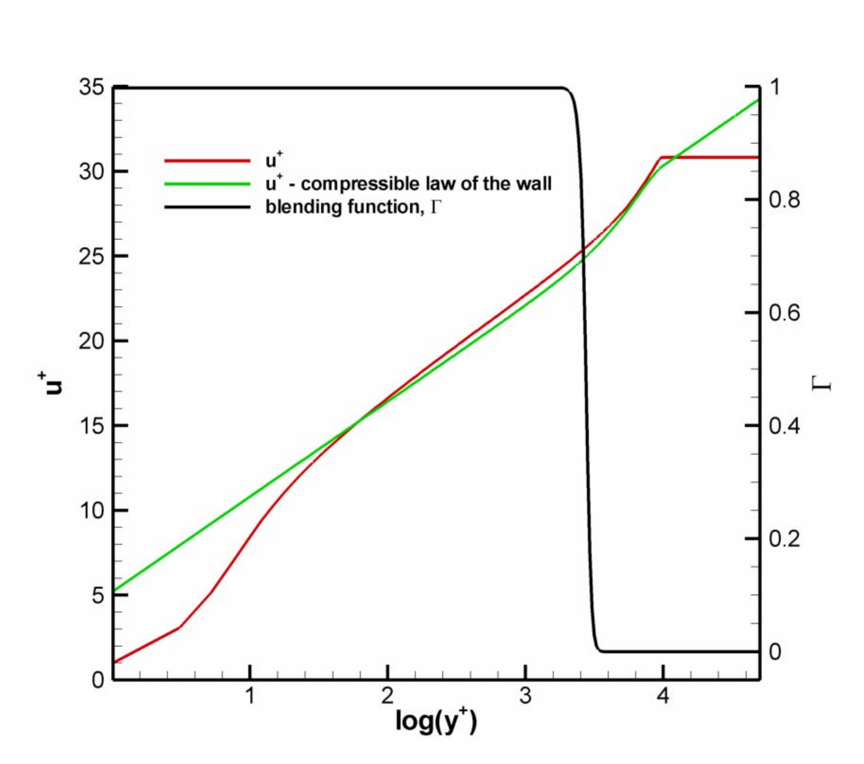

Figure 2.1.1: Blending function and velocity profile in wall coordinates

above accurately captures mean and second-moment compressible boundary-layer statistics over a wide range of Reynolds numbers, provided that the outer layer is resolved adequately (15-20 cells / boundary layer thickness in all directions).

2.2. New LES/RANS model development

Our development of a new LES/RANS model centers on the construction of an alternative form for the blending function that does not need a problem-specific calibration. There are problems with using the Taylor microscale as a representative turbulence length scale far away from the wall. At high Reynolds numbers, outer-layer statistics (when scaled properly) should be independent of Reynolds number and thus of the molecular viscosity. What is needed is a <u>local</u> estimate of the outer-layer integral scale (proportional to the boundary layer thickness). Equating this value with the inner layer integral scale (proportional to the wall distance) will give a reasonable estimate of the location of the outer part of the logarithmic region, and by analogy, a location where one might wish to shift the model response from RANS to LES. The difficulty is that the LES model locally supplies only inner-layer length scales (the wall distance + viscous length scales) and the grid scale.

The turbulence transport equations may provide some outer-layer length-scale information. As one example, the length scale that is naturally determined from a k-ω model is

$$l_{k-\omega} = \frac{k^{1/2}}{C_\mu^{1/4}\omega} \tag{2.2.1}$$

This length scale approaches the inner scale κd in the logarithmic region and decays toward zero in the outer part of the boundary layer and in the viscous sublayer. Taking the ratio of $l_{k-\omega}$ to the inner scale and adding in a viscous velocity scale proportional to $\nu\omega$ gives a potential form for the argument of a new blending function:

$$\lambda = \frac{\sqrt{10\nu\omega + k}}{C_\mu^{1/4}\kappa d\omega}, \tag{2.2.2}$$

with the constant (10) being chosen small enough so that the behavior of λ in the logarithmic and outer layers is not significantly influenced by the viscosity. The length-scale ratio λ should approach one and larger in the inner layer and should decay toward zero in the outer part of the boundary layer. The Menter k-ω model itself uses a ratio similar to λ to define its F_1 function. The delayed detached-eddy simulation (DDES) model [6] also uses a similar function to separate attached boundary layers from free-stream regions, and some of our earlier attempts at LES/RANS model development also used this basic form. An advantage of this form is that there is a good correlation between a particular value of λ and the 50% value of Γ as determined through the original calibration procedure. Figure 2.2.1 shows this for the three boundary layers considered in Ref. [2]. The length scale ratio in this figure is $L_\Gamma = \lambda^2$. These results show that the 50% value of the blending function correlates approximately with a value of $L_\Gamma = 0.6$ and is nearly independent of Reynolds number.

There are several problems, however, with the direct use of λ, evaluated using instantaneous values for ν, ω, and k. First, as shown in Figure 2.2.1, the decay rate of the function in the outer part of the boundary layer is rather slow. If the goal is to transition at the outer edge of the logarithmic region so that most of the boundary layer is modeled as a LES, then the functional form must be sharpened in some manner so that the decay rate is increased. Forms for the blending function that may be considered include

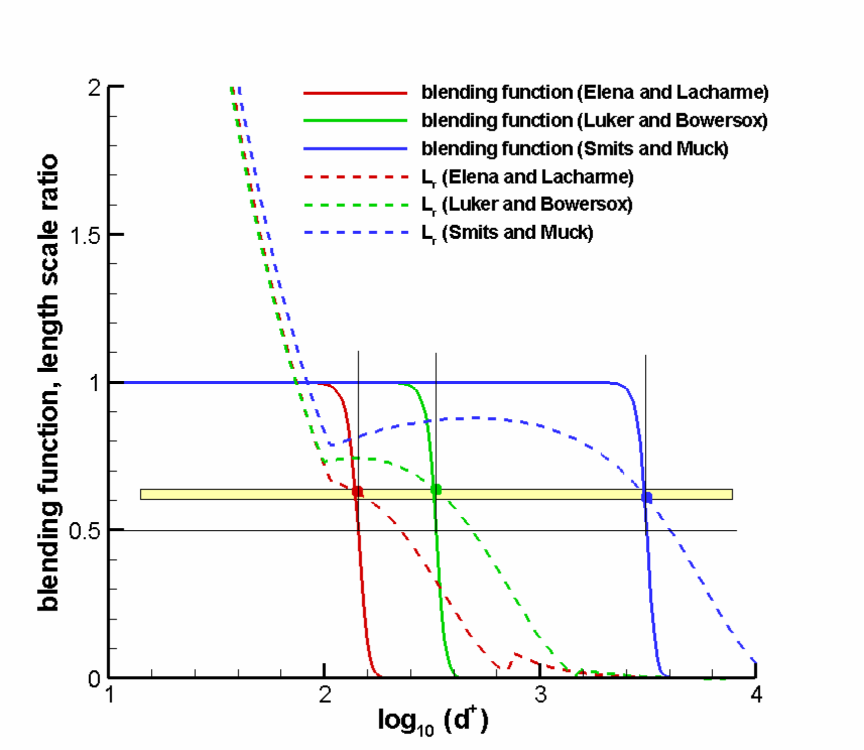

Figure 2.2.1: Correlation between blending function and length-scale ratio for several flat plate boundary layers

$$\Gamma = \frac{1}{2}\left(1 + \tanh[\, C(\lambda^k - D)]\right) \text{ or} \tag{2.2.3}$$

$$\Gamma = \frac{1}{2}\left(1 - \tanh[\, C(\frac{1}{\lambda^m} - D)]\right) \tag{2.2.4}$$

where C is the sharpening factor (normally > 5), D is the value for which Γ=0.5 (the RANS-to-LES transition 'point'), and m is a power.

The other problems are more subtle. Because the solutions for k and ω, as driven by an unsteady velocity field, are intrinsically noisy, local values for the length-scale ratio may differ substantially from the time-averaged values, which themselves may differ significantly from those expected from a RANS-based analysis (as used in Figures 2.1.1 and 2.2.1). There is also a strong coupling between the length scale ratio, the blending function, and the transport equations themselves. The functional form for the eddy viscosity (Eq. 2.1.3) depends on Γ, which itself depends on k and ω. The presence of Γ in the turbulence kinetic energy transport equation, in particular, induces a large damping effect for turbulence production, which causes the solution for k to be smaller than the RANS value (even where Γ may be one locally). This can be easily seen by writing the production term as

$$\mu_t S^2 = [\Gamma \rho \frac{k}{\omega} + (1-\Gamma)\rho \nu_{t,sgs}]S^2 = \rho \frac{k}{\omega} S^2 - (1-\Gamma)\rho(\frac{k}{\omega} - \nu_{t,sgs})S^2 \tag{2.2.5}$$

A consequence of this strong coupling and the diminishing of k near the RANS/LES interface is that the fixed-point solution of the LES/RANS equations (determined by the position of the time-averaged blending function within the boundary layer) may depend on the initial distribution of k. If, for example, a RANS solution is used to initialize k, the most probable response will be that the blending function stays near one throughout much of the boundary layer, meaning that turbulent fluctuations will be attenuated significantly. This is the operational mode required in DDES and related techniques, which seek to treat the entirety of an attached turbulent boundary layer as (unsteady) RANS. If the initial distribution for k is scaled so that the outer-layer value is near zero, then the $\Gamma = 0.5$ position blending function may stay initially near its target location, but will likely move toward the wall as the resolved turbulence intensity in the outer layer increases.

The original blending-function model described in the previous section avoids some of these difficulties in that it is a function of ω and not k, the former only being sensitive to the eddy viscosity through the diffusion terms and to k through the cross-derivative term. Thus, the model yields stable fixed-point solutions for the time-averaged position of the blending function. However, because of the absence of outer-layer length scale information, the original model cannot be self-adjusting and requires problem-specific calibration.

In this work, we propose a definition of the length scale ratio that avoids some of the above issues. Instead of only using the modeled k to define the ratio, we include the resolved turbulence kinetic energy $\bar{k}_R$, which is obtained by ensemble averaging the unsteady flow field according to

$$\bar{\rho}\bar{k}_R = \frac{1}{2}(\overline{\rho u_k u_k} - \frac{\overline{\rho u_k}\,\overline{\rho u_k}}{\bar{\rho}}) \tag{2.2.6}$$

The length scale ratio that results is

$$\lambda_N = C_N \frac{\sqrt{10\nu\omega + k + \bar{k}_R}}{C_\mu^{1/4}\kappa d\omega}, \tag{2.2.7}$$

with C_N being a model constant. The inclusion of the resolved turbulence kinetic energy ensures that part of the outer-layer length scale estimate is more independent of the positioning of the blending function within the boundary layer. An additional modification can be made to reduce the noise in the length-scale ratio to levels found in the original model:

$$\lambda_N = C_N \sqrt{10 + \frac{\bar{k} + \bar{k}_R}{\nu\bar{\omega}}} \frac{\sqrt{\nu}}{C_\mu^{1/4}\kappa d\sqrt{\omega}} \tag{2.2.8}$$

Here, we factor out the quantity $\sqrt{\nu\omega}$ and evaluate the component $\sqrt{10+\frac{\bar{k}+\bar{k}_R}{\nu\varpi}}$ using ensemble-averaged data for ω and k. The new blending function uses Eq. 2.2.8 in conjunction with Eq. 2.2.4 (with $C = 15$, $D = 1$, and $m = 2$):

$$\Gamma_N = \frac{1}{2}\left(1 - \tanh[\,15(\frac{1}{\lambda_N^2} - 1)]\right) \tag{2.2.9}$$

In this form, it is easy to compare the new blending function with the original. One can re-write the original form into that of Eq. 2.2.4:

$$\begin{aligned}\Gamma_o &= \frac{1}{2}[1 - \tanh(\{5 + \tanh^{-1}(0.98)\}(\frac{5}{5 + \tanh^{-1}(0.98)}\frac{\kappa}{C_\mu^{1/2}(\alpha_1)^2}\left(\frac{d}{\chi_T}\right)^2 - 1)] \\ &= \frac{1}{2}[1 - \tanh(7.30(\frac{\kappa}{1.46C_\mu^{1/2}(\alpha_1)^2}\left(\frac{d}{\chi_T}\right)^2 - 1)]\end{aligned} \tag{2.2.10}$$

Introducing the Taylor microscale into Eq. 2.2.10, one can write the new blending function as

$$\Gamma_N = \frac{1}{2}[1 - \tanh(15(\frac{1}{C_N{}^2(10 + \frac{\bar{k}_R + <k>}{\varpi\nu})}\frac{\kappa^2}{C_\mu^{1/2}}\left(\frac{d}{\lambda_T}\right)^2 - 1)] \tag{2.2.11}$$

Equating the denominators in the arguments of the original and new blending function, it is easy to see that

$$\alpha_1{}^2 \approx \frac{C_N^2}{1.46\kappa}(10 + \frac{\bar{k}_R + <k>}{\varpi\nu}) \tag{2.2.12}$$

In essence, the new model replaces the problem-specific constant α_1 with a form that varies in space and also in time, as the ensemble averages may not be time-invariant and as the kinematic viscosity is a local quantity. The model constant C_N must be obtained through numerical experiments. Considering the same three compressible boundary layers as in [2] and comparing mean- and second-moment statistics with those obtained using the original model (results shown later), we have determined that a value of $C_N = 1.5$ gives acceptable results. Figure 2.2.3 plots the quantity $\left(\frac{C_N^2}{1.46\kappa\alpha_1{}^2}(10 + \frac{\bar{k}_R + <k>}{\varpi\nu})\right)^{1/2}$ versus the normalized wall distance for each of the boundary layers considered in [2]. The values of α_1 for the Elena and Lacharme [7], Luker, et al.[8], and Smits and Muck [9] experiments are 14.16, 23.22, and 75.24, respectively. The peak values for each distribution are close to unity but are lower than unity where the RANS-to-LES transition takes place ($y/\delta \sim 0.2$). Also shown in Figure 2.2.3 are the time-averaged blending functions for the new model and for the original model. In general, the $\Gamma = 0.5$ values are closer to the wall for the new model, but the transition zone itself ($0 < \Gamma < 1$) is broader.

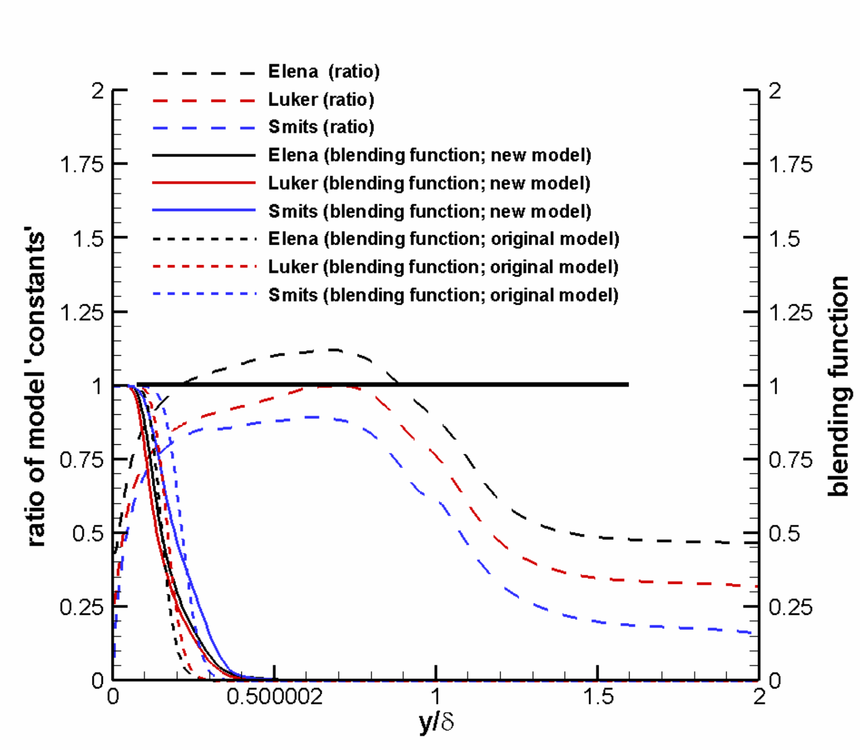

Figure 2.2.3: ratio of model 'constants' and blending function distributions versus normalized wall distance for three compressible boundary layers

2.3. Model modifications

Since the original development of the new model, there have been some modifications made to allow some control over the RANS-to-LES transition. In some problems, there is a need to guarantee operation in RANS-mode for various reasons, such as the lack of sufficient mesh resolution for resolving fluctuations or a user's choice to not attempt to resolve fluctuations in certain regions of the flow. The calibration of the current LES/RANS model assumes that sufficient resolution is present and that only the inner 20% or so of a boundary layer will require some level of RANS modeling. The model therefore does not work properly in situations where a.) resolved turbulence is not sustained through some procedure, or b.) the mesh resolution isn't adequate to support resolved turbulence. Two methods for controlling the transition have been developed and are described in this section. The first method modifies the blending function argument as follows:

$$\Gamma = \frac{1}{2}\left(1-\tanh[15(\frac{1}{\lambda_N^2}-\frac{1}{\beta})]\right), \qquad \beta = \max[\beta_0, \max_k(C_k \min(1,\frac{d}{d_k})] \tag{2.3.1}$$

Here, β is a function of distance functions d_k as calculated from a user-specified number (k) of solid surfaces and the global distance function d. The user determines beforehand whether a surface is to be treated as a 'RANS wall' (C_k= 0) or as a 'LES wall' (C_k= 1). This function approaches one for cells near a 'LES wall' and approaches a threshold value β_0~0.05 for cells near a 'RANS wall'. The effect is to shift the RANS-to-LES transition location toward the outer edge of a boundary layer when one does not wish to resolve turbulence within that boundary layer.

The second method determines adequacy of the mesh resolution by comparing the estimated outer-layer length scale with the maximum mesh scale according to the following:

$$\lambda_N = g(l_{outer})l_{outer}/l_{inner}\,, \quad g(l_{outer}) = \min[D_1, \max(1, D_2 \frac{\Delta_{\max}}{l_{outer}}\sqrt{\frac{\overline{\omega}}{\omega}})] \tag{2.3.2}$$

where

$$l_{outer} = C_N \sqrt{\frac{10\nu\overline{\omega} + \overline{k} + \overline{k}_R}{C_\mu^{1/2}\overline{\omega}\omega}}, \quad l_{inner} = \kappa d \tag{2.3.3}$$

The model constants D_1 and D_2 are assigned values of 10 and 0.5, based on calibrations for flat-plate boundary layers. The mesh scale $\Delta_{\max}$ is taken to be the maximum spacing over all three coordinate directions. This form serves to shift the closure to unsteady RANS when there is no possibility of resolving the largest turbulence length scales. If the maximum mesh scale is selected as the outer-layer scale consistently, then the LES/RANS model behaves similarly to detached-eddy simulation, serving primarily to isolate turbulent boundary layers from massively-separated regions. Figure 2.3.1 shows the effective RANS to LES transition position as a function of the maximum mesh spacing for a flat-plate boundary layer. As the mesh spacing gets larger than ~10% of the boundary layer thickness, the transition location moves outward and the model shifts more to unsteady RANS.

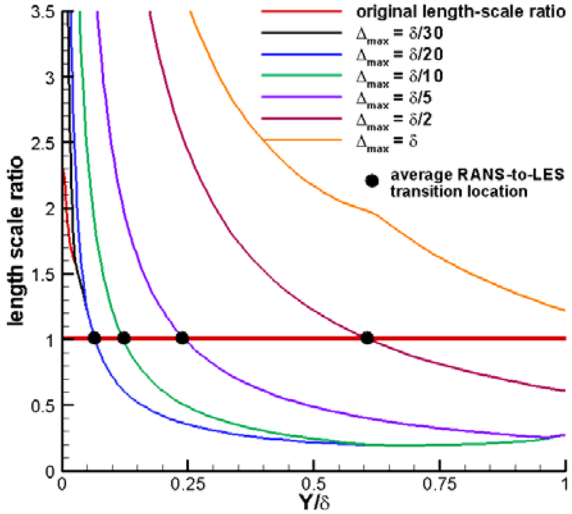

Figure 2.3.1: Length-scale ratio versus Y/δ (Elena and Lacharme flat plate boundary layer)

2.4. Ensemble averaging

The new LES/RANS model requires ensemble-averaging of unsteady data to form the turbulent length-scale ratio required for the blending function. These ensemble averages are currently computed using an exponentially-weighted moving average: $\overline{Q}^n = (1-A)\overline{Q}^{n-1} + AQ^n$ with $A = \Delta t/\tau$. The time scale τ is defined as follows for each of the variants considered in this study:

$$\begin{aligned} &1.\quad \tau = t \\ &2.\quad \tau = \min(t, t_{res}),\ t < 4t_{res} \\ &\qquad\ = t - 3t_{res}, t \geq 4t_{res} \\ &3.\quad \tau = \min(t, t_{res}) \end{aligned} \tag{2.4.1}$$

where $\tau_{res} = L / u_\infty$ is defined in terms of the length of the domain L and the free-stream velocity u_∞ Method 3 is an exponentially-weighted moving average, with the 'window' set as one flow-through time, while Method 1 is a conventional time average. Method 2 is a blend of a 'windowed' average and a conventional one. Results illustrating the effect of these variations are described later in this document.

3. Model Assessment: Flat Plate Boundary Layers

3.1. Baseline predictions

Three supersonic flat-plate boundary layers experiments were simulated to calibrate the new model and to assess the sensitivity of the model to the model constants and to the method of ensemble-averaging. Figures 3.1.1-3.1.3 compare predicted mean velocity, Reynolds shear stress, and *rms* normal and axial fluctuation intensities with experimental data [10-12]. The constant C_N is set to 1.5 for the new model, while the constant C_S is chosen as 15 and as 5. Reynolds numbers based on the boundary layer thickness are 5.59e4, 1.78e5, and 1.58e6 for the Elena and Lacharme [10], Luker, et al. [11], and Smits and Muck [12] experiments, respectively. The meshes each contain 5.12 million cells and are designed so that approximately 20 cells / boundary layer thickness are present in the wall-transverse directions (x and z). Significantly more resolution (>100 cells / boundary layer thickness) is present in the wall normal direction. Calculations using the original model [7] are also presented. These results show several trends. First, the mean velocity is relatively unaffected by the model choice. The Reynolds shear stress distributions, presented in terms of their modeled and resolved components, show that the decay in resolved Reynolds shear stress is compensated for by an increase in the modeled component. The 50% value in the normalized modeled Reynolds stress corresponds approximately to the 50% value in the time-averaged blending function. With the exception of the Smits and Muck case, the differences among Reynolds-shear stress profiles predicted by each model are small. Lowering the sharpening factor from 15 to 5 leads to an increase in the modeled Reynolds shear-stress component, implying that the position of the time-averaged RANS-to-LES transition shifts

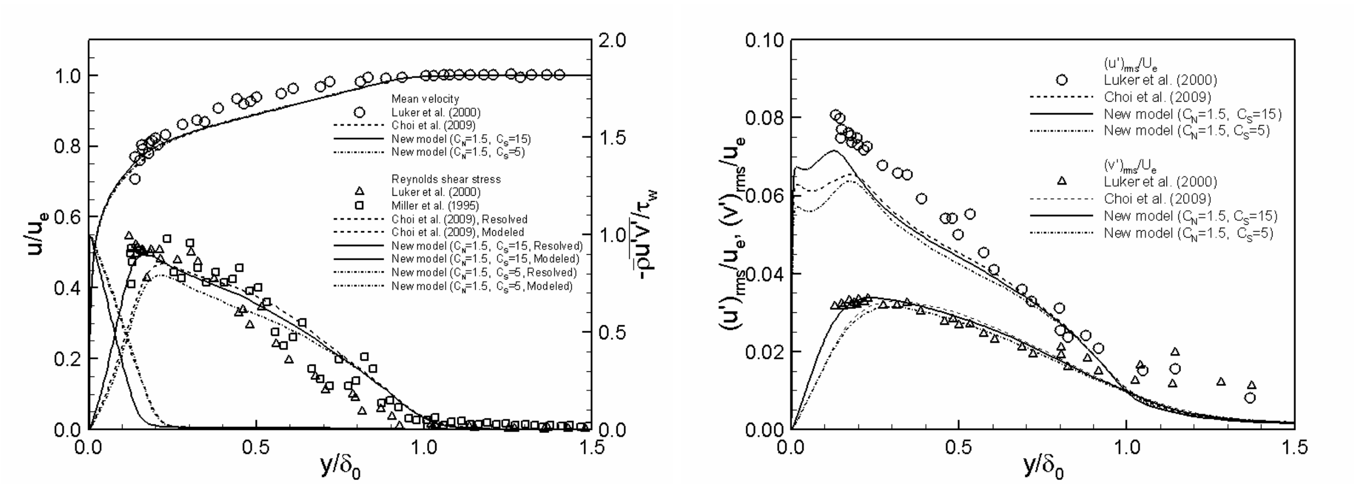

Figure 3.1.1: Mean velocity, Reynolds shear stress, *rms* axial velocity, and *rms* normal velocity versus normalized wall distance (Luker, et al. experiment)

further away from the wall. All models under-predict the peak in *rms* axial velocity indicated in all datasets at $y/\delta_0 < 0.2$. This appears to be a consequence of the damping effect of the RANS component of the model. It should be noted that the modeled contributions to the Reynolds normal stresses are not included in the *rms* velocity comparisons, as the Boussinesq approximation is known to be invalid for these components in the near-wall region. With the exception of the Smits and Muck case, the model predictions for the *rms* normal velocity are in good agreement with experimental data. In all cases, the predictions provided by the new model are comparable to those of the original model.

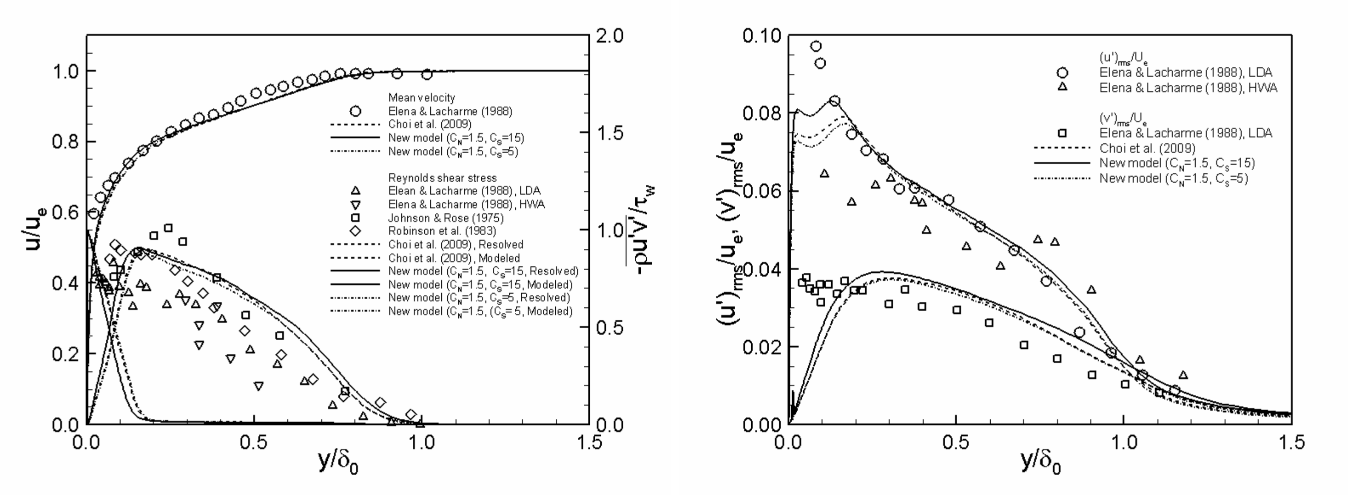

Figure 3.1.2: Mean velocity, Reynolds shear stress, rms axial velocity, and rms normal velocity versus normalized wall distance (Elena and Lacharme experiment)

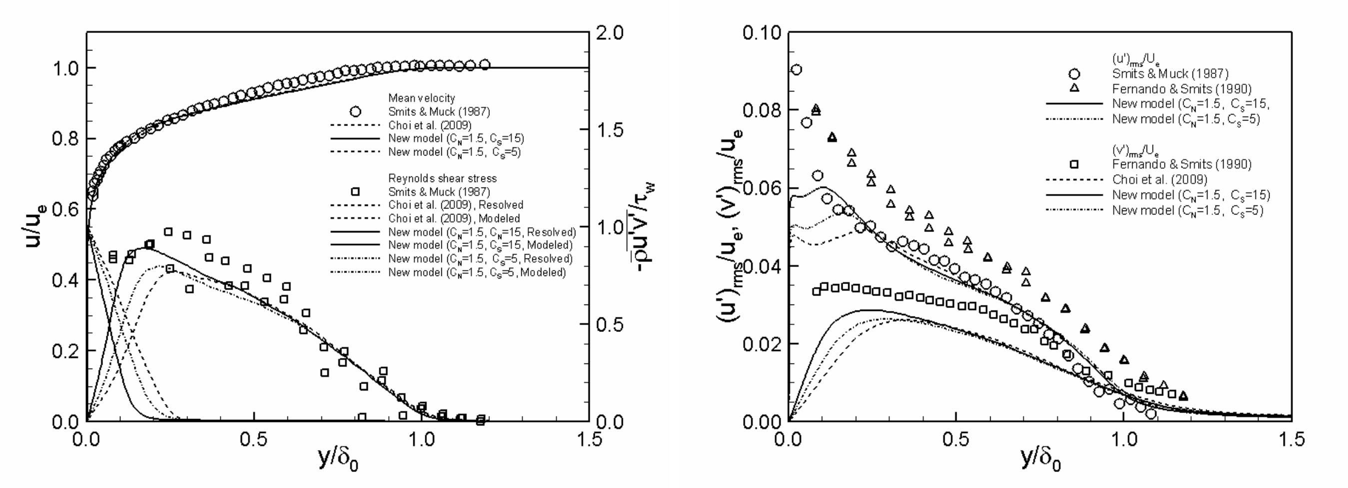

Figure 3.1.3: Mean velocity, Reynolds shear stress, *rms* axial velocity, and *rms* normal velocity versus normalized wall distance (Smits and Muck experiment)

3.2. Sensitivity to C_N

Figure 3.2.1 addresses the sensitivity of the predictions to variations in the model constant C_N. The experiment of Luker, et al. is considered in this evaluation. As expected, a trend of increasing the modeled Reynolds shear-stress component and decreasing the resolved component is evidenced with an increase in the model constant. As the model constant reduces, more of the resolved turbulence energy near the wall is captured, and the prediction of *rms* axial velocity, in particular, improves. This effect is accompanied, however, by an increase in the fullness of the velocity profile in the outer part of the logarithmic region ($0.1 < y/\delta_0 < 0.25$) and, as shown later, a decrease in the wall shear stress. The apparent over-prediction of the resolved Reynolds shear stress for $C_N = 1.2$ is partly a result of this reduction in the wall stress. Even at the highest value of C_N considered (2.2), a significant amount of fluctuation energy is still sustained in the outer layer. A shift to a RANS-like response would require even larger values of the model constant.

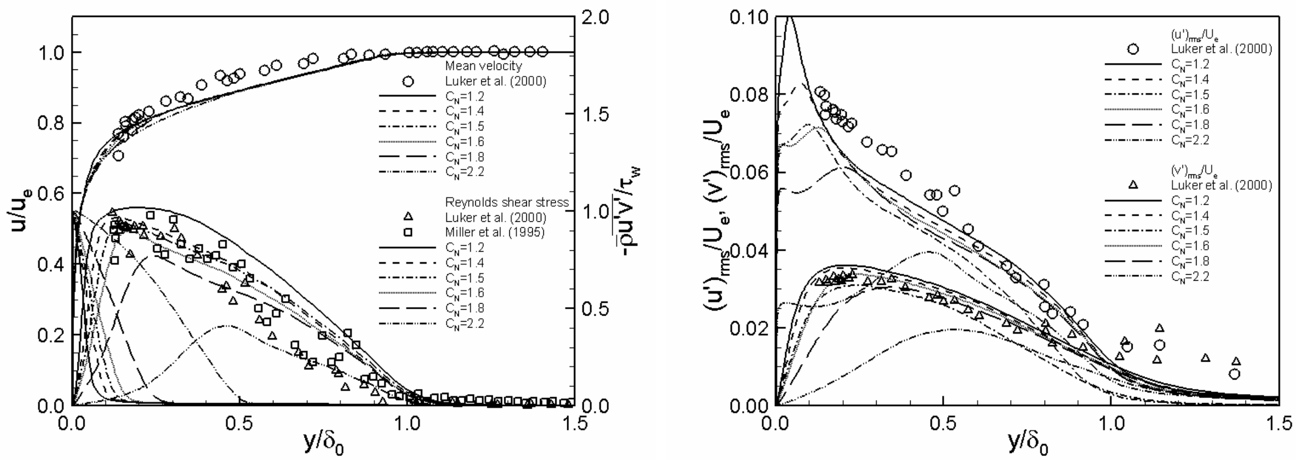

Figure 3.2.1: Effect of C_N (Luker, et al. experiment)

3.3. Sensitivity to ensemble-averaging method and C_S

The sensitivity of the predictions to the method of ensemble-averaging and to the selection of C_S is illustrated in Figures 3.3.1a and 3.3.1b, corresponding to the Luker, et al. and Smits and Muck experiments. Comparisons with experimental data are again presented for the resolved Reynolds shear stress, but the velocity profiles are shown in inner-layer coordinates using the Van Driest I transformation. This transformation highlights the smoothness of the velocity profile in the inner region and indicates the degree to which a 'log-law mismatch' is observed. The sensitivity of the predictions to the method of ensemble-averaging is not high, but the conventional average ("Weighting #1") places the time-averaged RANS-to-LES transition somewhat further away from the wall. This implies that some of effects of the initial distribution of turbulence variables are maintained when conventional averaging is used. Weightings #2 and #3 provide very similar solutions for both cases. A severe log-law mismatch is not observed in any case, but the velocity profile is not completely smooth, exhibiting a small hump that is reduced in size as the time-averaged transition position shifts further away from the wall. A lower value of C_S also seems to promote a smoother profile. In all cases, the computed profiles in the logarithmic and wake regions lie above the theoretical solution. This is a consequence of a slight under-prediction of the wall shear stress exhibited by all models tested.

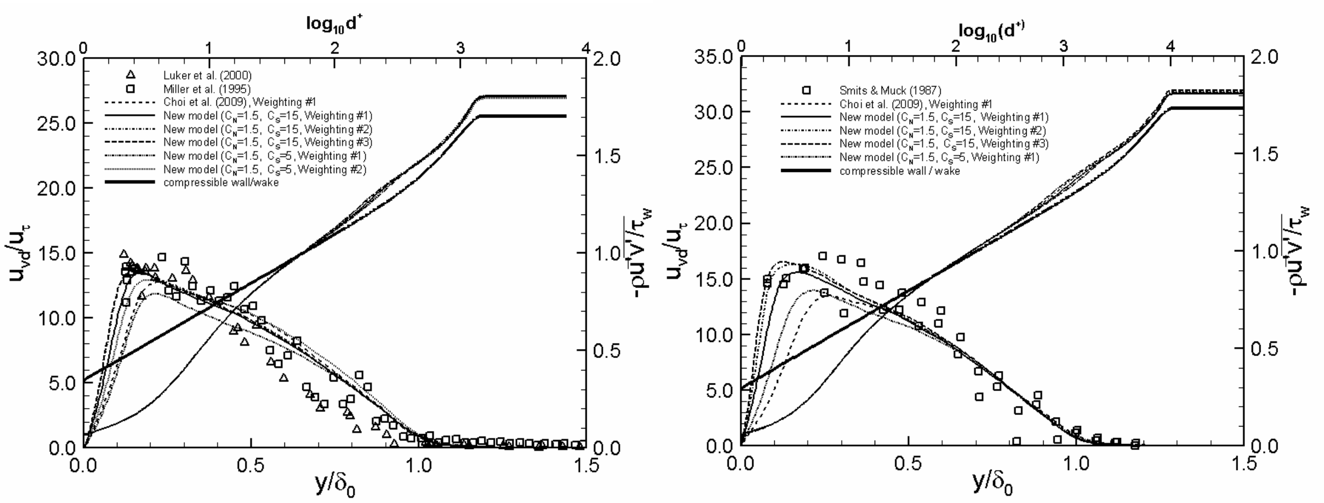

a.) Luker, et al. b.) Smits and Muck

Figure 3.3.1: Effect of ensemble-averaging technique and C_s

3.4. Comparison with IDDES

An alternative wall-modeled LES strategy (termed IDDES) has been developed by Shur, et al. [10] as an extension of the delayed detached-eddy simulation (DDES) model.[6] Variants based on the Menter SST model and the Spalart-Allmaras model have been formulated. The general idea adopted by IDDES is that the mesh spacing, plus the presence of initial fluctuation content, will dictate whether the model responds as a wall-modeled LES, as DDES, or as a pure RANS model. It is thus a more general framework than our model, which is strictly a type of wall-modeled LES. The wall-modeled LES branch of IDDES differs from ours in several respects. First, the Menter-SST model is used as the basis, rather than the Menter BSL model. Secondly, only the destruction term in the turbulence kinetic energy equation is modified through the action

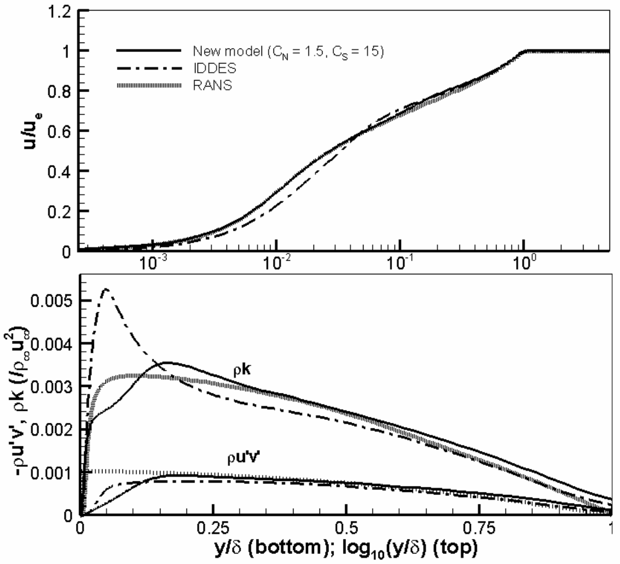

Figure 3.4.1: Reynolds-shear stress, turbulence kinetic energy, and mean velocity predictions for different turbulence models (Elena and Lacharme experiment)

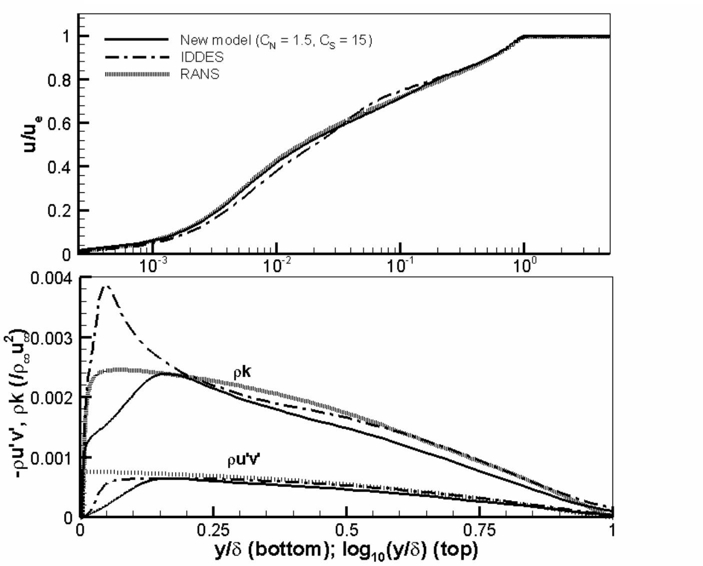

Figure 3.4.2: Reynolds-shear stress, turbulence kinetic energy, and mean velocity predictions for different turbulence models (Luker, et al. experiment)

of a blending function. The eddy viscosity responds to the combined influences of the turbulence kinetic energy, the turbulence frequency, and a specified filter width – there is no separate SGS eddy viscosity. In our model, the eddy viscosity description is designed to shift between RANS and LES branches, and in principle, different SGS and RANS models could be employed. The blending functions used in IDDES are fundamentally based on the ratio of the wall distance to a filter width, and thus the transition between RANS and LES branches occurs at fixed locations for a particular grid. In our model, the instantaneous transition location will migrate in response to the resolved and ensemble-averaged solution. The IDDES method uses flow-dependent 'enhancement' functions to augment the RANS component in the vicinity of the transition location – the authors argue that such functions are crucial for combating 'log-law mismatch'. For the array of flat-plate boundary layers considered in this work, the transition location as calculated in the IDDES model is at $y/\delta_0=1/40$. In wall coordinates, this places the transition at $d^+ = 17.8$, 36.7, and 251.8 for the Elena and Lacharme, Luker, et al, and Smits and Muck cases, respectively The first two locations are near the beginning of the logarithmic region, while the latter is more toward the middle of the region.

Figures 3.4.1-3.4.3 compare solutions obtained using the new model ($C_N = 1.5$, $C_S = 15$) with those from IDDES and with Menter BSL RANS solutions for each of the three cases. The RANS velocity solutions agree very well with the compressible law of the wall and with the experimental data and thus might be used as a reference to assess the predictive capability of the other models. The resolved turbulence kinetic energy and Reynolds shear-stress are plotted for the LES/RANS models, while the modeled turbulence kinetic energy and Reynolds shear-stress are plotted for the RANS model. The axial velocity is plotted versus $\log_{10}(y/\delta_0)$ and is scaled by the free-stream velocity instead of the friction velocity. This removes ambiguities associated with the possible under-prediction of the wall shear stress. Both LES/RANS models predict outer-layer values of turbulence kinetic energy and Reynolds-shear stress that are comparable to those modeled using RANS. The model responses differ greatly in the inner layer, with the

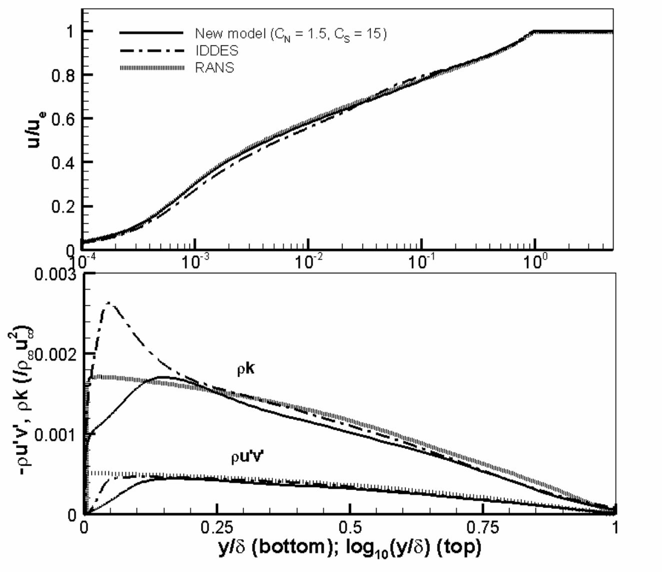

Figure 3.4.3: Reynolds-shear stress, turbulence kinetic energy, and mean velocity predictions for different turbulence models (Smits and Muck experiment)

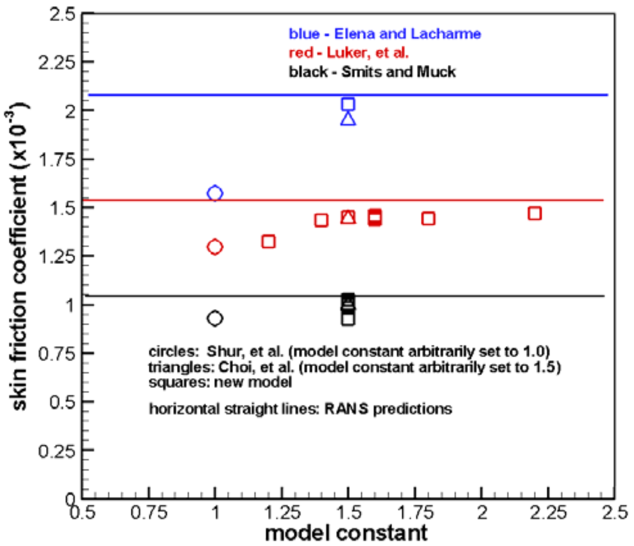

Figure 3.4.4: Skin friction vs model constant

IDDES solution exhibiting a peak in turbulence kinetic energy also captured in the C_N = 1.2 solution of Figure 3.2.1. The rapid diminishing of the resolved fluctuation energy near the wall by the new model is again in evidence. The new LES/RANS model predicts velocity profiles that are in close accord with the RANS solutions, whereas the IDDES solutions show an increase in velocity toward the outer part of the logarithmic region followed by a decrease in velocity in the inner part of the layer. Figure 3.4.4 presents a scatter plot of predicted skin friction versus C_N for all of the models considered in this study. For IDDES, C_N is arbitrarily set to one, while for Choi, et al, C_N is set to 1.5. The general trend is that all of the LES/RANS models under-predict the wall shear stress level (as provided by the RANS model), with the IDDES and C_N = 1.2 solutions showing the largest deviations. Based on these results and the others presented, it appears that a RANS-to-LES transition that occurs near the inner edge of the logarithmic layer can result in insufficient dissipation of resolved turbulence energy in the outer part of the logarithmic layer. Axial fluctuation-intensity predictions improve, but inaccuracies in the wall shear stress and inner-layer velocity profile appear. Shifting the RANS-to-LES transition toward the middle and outer parts of the logarithmic layer, as is done in the new model with C_N =1.5-1.6, yields closer agreement with theory and with RANS predictions for the velocity profile but leads to an under-prediction of the resolved axial fluctuation intensity in the near-wall region. Figure 3.4.5 shows that the differences between the predictions of the new model and those of IDDES are not likely to be a result of the SGS component of the closure. The normalized eddy viscosity is much larger for IDDES in the outer layer, where the SGS model should be most active. The opposite situation occurs close to the wall. The degree to which these observations are also a function of the behavior of the current numerical method is unknown, and the sensitivity of the predictions to mesh refinement remains to be assessed. It is unlikely, however, that practical LES/RANS calculations using meshes finer (in terms of cell size per shear layer thickness) than those considered herein will be affordable in the near term, but the methods should be assessed for coarser levels of resolution (10 to 15 cells / shear layer thickness).

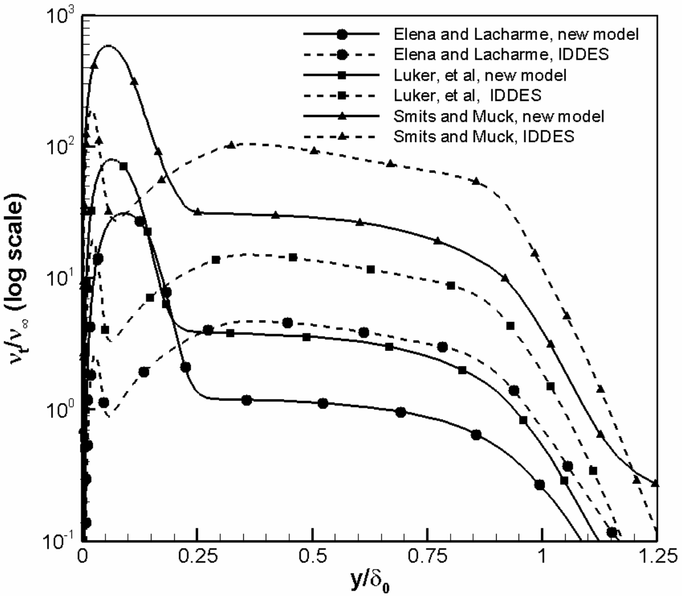

Figure 3.4.5: Normalized kinematic eddy viscosity distributions – new model and IDDES

4. Model Assessment: 16 degree Smooth Compression Ramp

The LES/RANS models have been applied to a Mach 2.86, 16-degree smooth compression-corner interaction mapped by Donovan, et al. [11,12] The flow conditions for this case and the previously-discussed flat-plate cases are shown in Table 4.1. The specific variants tested are the original model of [2] (with the model constant $\alpha_1 = 13.06\,s + 76.7$ fitted as a function of the surface coordinate s), the new model with $C_N = 1.5$ and $C_s = 15$ using Weighing #1 for ensemble averaging, and the new model with $C_N = 1.5$ and $C_s = 15$ using Weighing #2 for ensemble averaging (See Section 2.4). The mesh extends from X = -0.28 m to X = 0.2717 m in the streamwise direction, with X = 0 m corresponding to the start of the 16 degree turn. The mesh extends 0.14 m in the wall-normal (Y) direction and +/- 0.0756 m in the spanwise (Z) direction. The mesh resolution is such that 20 cells / incoming boundary layer thickness are present in the wall-transverse directions, and the total number of interior mesh cells is 8.64 M. The recycle plane is located 7.5 boundary-layer thicknesses (δ=2.5 cm) downstream of the inflow plane.

Table 4.1: Free-stream and boundary-layer properties for experiments considered in this study.

Case	M_∞	δ_0, mm	U_∞, m/s	Re_δ	P_o, pa	T_o, K	C_f $(\times 10^{-3})$
Elena and Lacharme [21]	2.32	10 (12)*	552	5.59×10^{4}	5.0×10^{4}	291	2.15
Luker, et al. [22]	2.80	9.9	602	1.78×10^{5}	2.1×10^{5}	298	1.6
Smits and Muck [23]	2.79	25	562	1.58×10^{6}	6.9×10^{6}	263	1.07
Donovan , et al. [16]	2.86	28	580	1.76×10^{6}	6.9×10^{6}	270	1.08

*- evaluated at 99.9% of boundary layer edge velocity

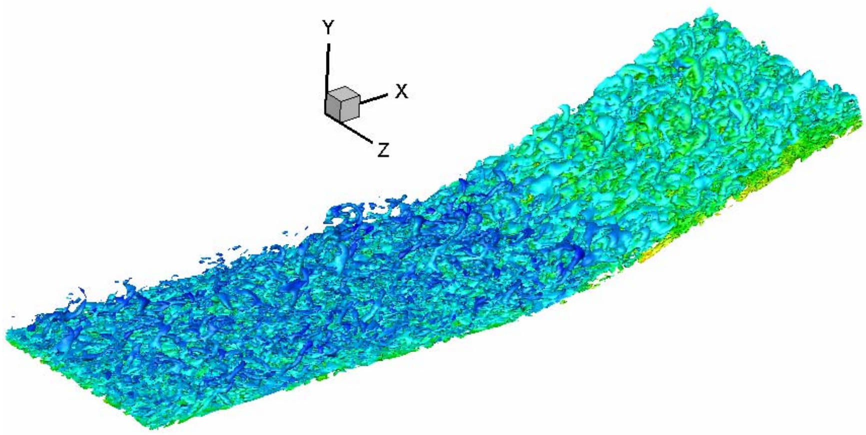

Figure 4.1.1: Iso-surfaces of swirl strength (7500 s-1) colored by temperature values (Donovan, et al. experiment)

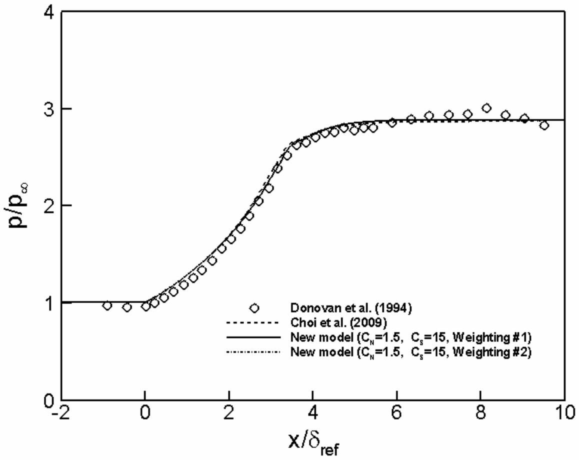

Figure 4.1.2: Surface wall pressure distributions (Donovan, et al. experiment)

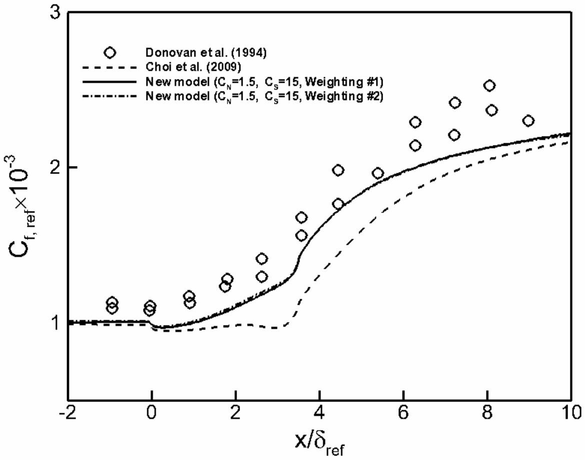

Figure 4.1.3: Surface skin friction distributions (Donovan, et al. experiment)

An iso-surface of swirl strength (7500 s^{-1}), colored by temperature, is shown in Figure 4.1.1 for the Donovan, et al. experiment. The swirl strength is defined as the imaginary portion of the complex eigenvalue of the local velocity gradient tensor. The higher the value of the swirl strength, the shorter the time required for a fluid particle to swirl about a vortex core. Higher values of the swirl strength typically correspond to smaller-scale turbulent structures, and the distribution of the swirl strength can provide an approximate measure of the distribution of the sizes of turbulent eddies. The value chosen (7500 s^{-1}) is large enough to highlight the presence of longitudinally-oriented vortical structures in the recovering boundary layer downstream of the isotropic compression. These appear to arise from amplification of inhomogeneities in the incoming boundary layer and have been observed in both experiments and computations of compression-ramp flows.

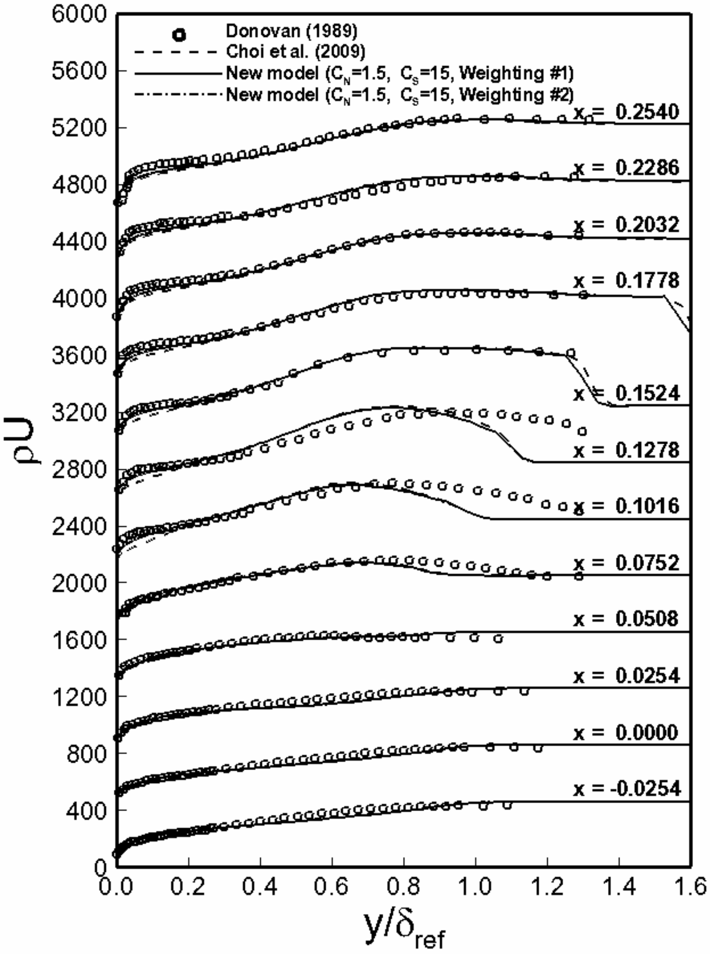

Figure 4.1.4: Streamwise mass flux distributions throughout the interaction region (Donovan, et al. experiment)

Predictions for mean-flow properties for the Donovan, et al. experiment are shown in Figures 4.1.2-4.1.4.

Time- and span-averaging of the instantaneous data is used to generate the mean values. Surface pressure distributions in Figure 4.1.2 show evidence of a smooth compression process unaffected by local flow separation. Figure 4.1.3 shows that, relative to the original model, the new LES/RANS model yields better agreement with surface skin friction measurements of Donovan within and downstream of the compression region.

Figure 4.1.4 compares mean mass flux distributions (based on the velocity component tangential to the surface) with experimental hot-wire data throughout the interaction. Good agreement is indicated in general, though the computed profiles do show an under-prediction of the mass flux distributions in the near-wall region downstream of the compression region. Locations in the flow field associated with the coalescence of compression waves into a shock wave (Figure 19, X = 0.1016 and X = 0.1278 stations) are also not well-predicted. The hot-wire measurements may not be as accurate in this region. The new model predicts a faster recovery of the inner part

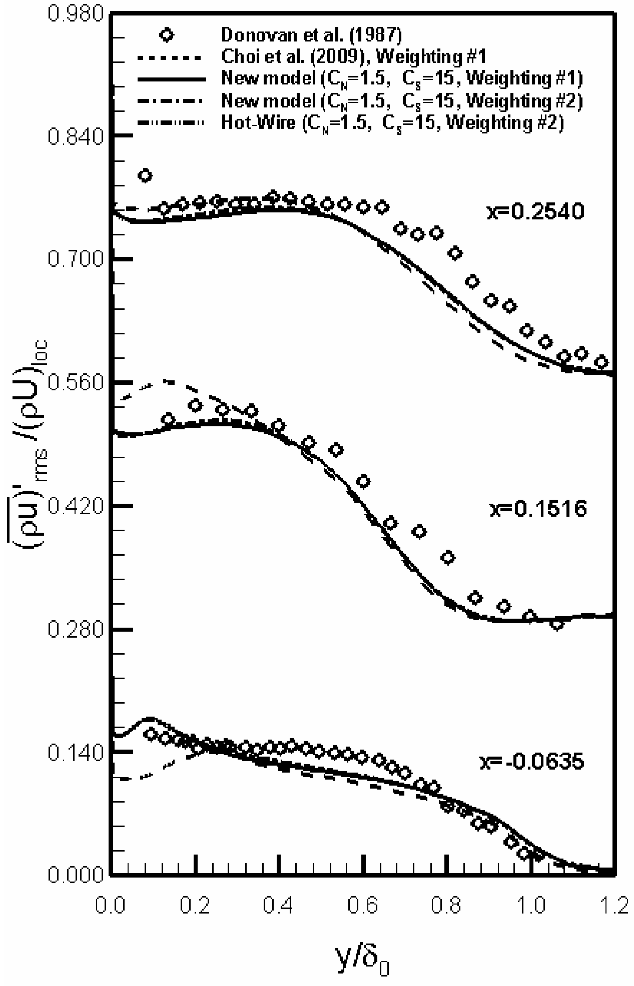

Figure 4.1.5: Mass flux fluctuation intensity profiles at different streamwise stations (Donovan, et al. experiment)

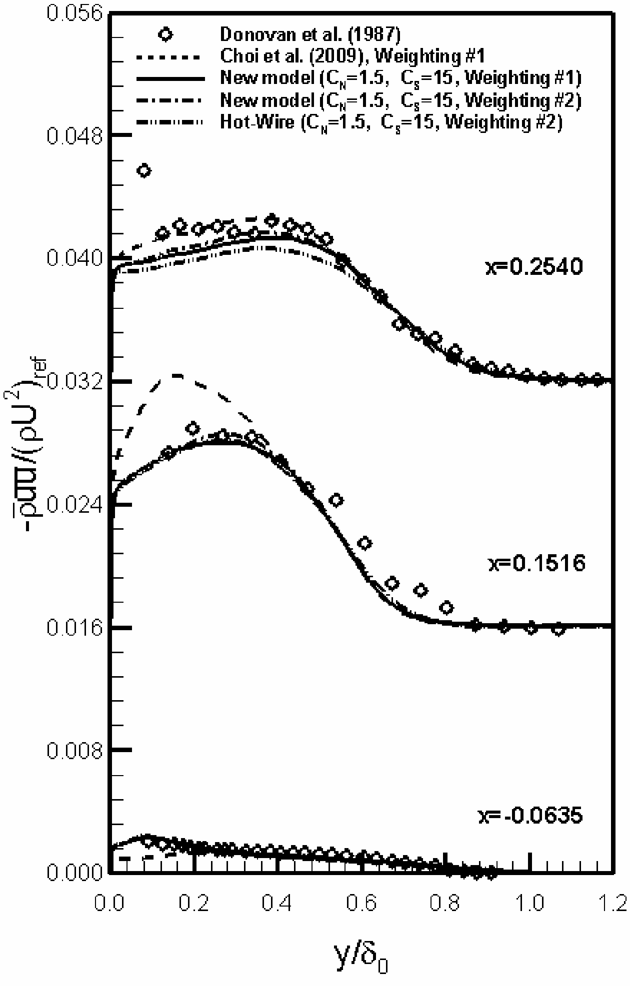

Figure 4.1.6: Reynolds axial stress profiles at different streamwise stations (Donovan, et al experiments)

of the boundary layer downstream of the compression region and provides slightly better agreement with experiment in this region.

Figure 4.1.5 compares mass-flux fluctuation intensity predictions with experimental data at three streamwise locations within the interaction region. The mass-flux fluctuation intensity is computed according to

$$\left(\overline{[(\rho\tilde{u}_1)']^2}\right)^{1/2} = [\overline{(\rho\tilde{u}_1)^2} - \overline{\rho\tilde{u}}_1\,\overline{\rho\tilde{u}_1}]^{1/2} \qquad (4.1.1)$$

where the overbar represents time and span-averaging of the grid-filtered data and $\tilde{u}_j$ is the velocity vector expressed in a coordinate system that is aligned with the compression-corner surface. At its peak in the incoming boundary layer, the maximum value of the mass flux fluctuation intensity is about 15%, increasing to a maximum of about 25% midway along the

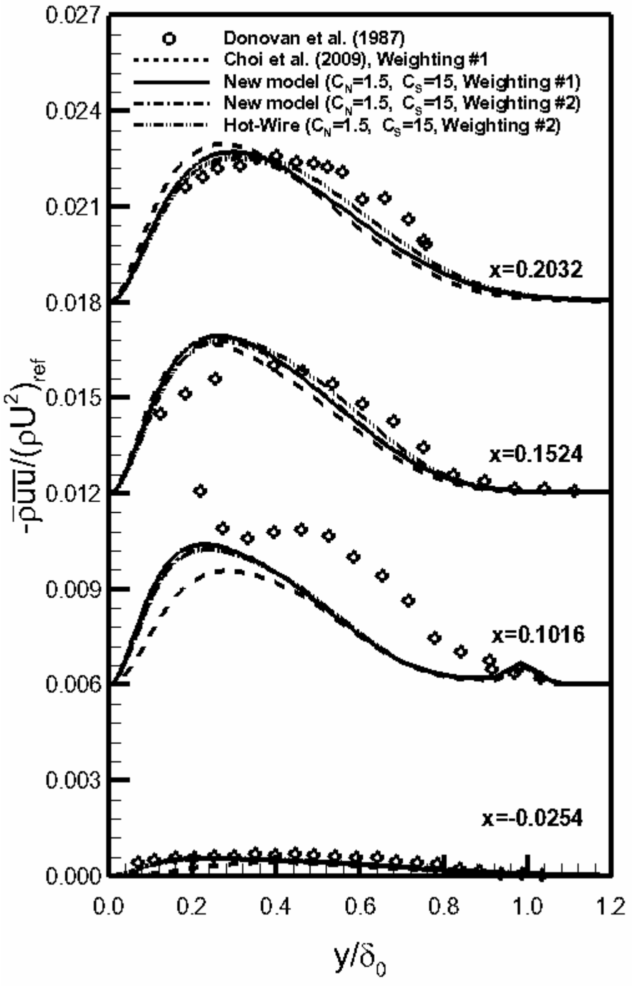

Figure 4.1.7: Reynolds normal stress profiles at different streamwise stations (Donovan, et al. experiments)

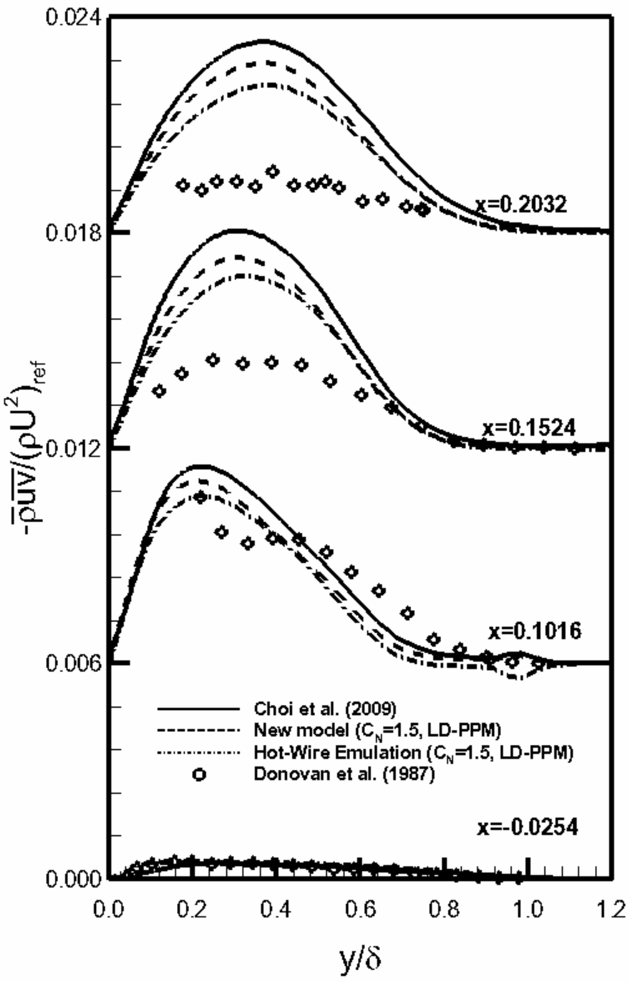

Figure 4.1.8: Reynolds shear stress profiles at different streamwise stations (Donovan, et al. experiments)

compression-ramp portion. As the boundary layer begins to relax back to a new equilibrium state, the mass flux fluctuation intensity diminishes. The LES/RANS predictions are in good agreement with experimental data at every station, with the new model providing better overall agreement nearer to the surface.

Favre-averaged Reynolds-stresses are computed according to

$$\bar{\rho}\overline{\tilde{u}_i''\tilde{u}_j''} = \overline{\rho\tilde{u}_i\tilde{u}_j} - \frac{\overline{\rho\tilde{u}}_i\,\overline{\rho\tilde{u}}_j}{\bar{\rho}} \tag{4.1.2}$$

Only the resolved Reynolds stresses are captured in this approach, but as the experimental data does not extend far into the wall layer, this is adequate for comparison. Figure 4.1.6 compares experimental measurements of the Reynolds axial stress with computational predictions. Good agreement is generally indicated, though calculations performed using the original LES/RANS model do over-predict the peak value of the Reynolds normal stress at the X = 0.1516 m data station, which is near the point where the isentropic compression ends. The new model provides improved results at this station. Evidence obtained from earlier shock impingement and compression-ramp studies indicates that the original model may over-amplify turbulent fluctuations in the near-wall region downstream of a strong compression. This problem may be related to a collapse in the blending function toward the wall, which enables larger turbulent eddies to interact with the wall without significant attenuation. The fact that the new model improves upon this response is encouraging.

Comparisons with the measured Reynolds normal stress (Figure 4.1.7) show that the trends regarding amplification of this component are in agreement with those shown in the experimental data and are consistent with those evidenced in Figures 4.1.5 and 4.1.6. Agreement with experiment is poor for the Reynolds shear stress (Figure 4.1.8), as the computations over-predict the measured values by more than a factor of two at the most downstream stations. The experimental data shows a marked decrease in the amplification rate of the Reynolds shear stress downstream of the end of the compression region. The calculations do not show this response, and neither the experimental data nor the computational predictions for the other Reynolds-stress components show such a rapid return to equilibrium.

5. Model Assessment: 20 degree Sharp Compression Ramp

5.1. Mean flow predictions

This section describes the application of the new LES/RANS model to Mach 3 flow over a 20-degree compression corner also studied at Princeton University. Velocity, wall-pressure, and skin friction measurements, along with hot-wire measurements of rms mass flux, Reynolds axial stress, and Reynolds shear stress are available for this case in the Supersonic / Hypersonic Shock Wave / Turbulent Boundary Layer Interaction Database [13]. This case differs from the Donovan and Smits experiment in that the oblique shock generated at the compression corner is strong enough to separate the incoming turbulent boundary layer. We have applied the new model (C_N = 1.5, C_S =15) to this case using ensemble-averaging weighting methods 1 and 2 as well as the original approach of Choi, et al. Figure 5.1.1 shows snapshots of temperature contours for the Choi, et al. model (PPM discretization) and the new model (LD-PPM, weighing method 2). Time-averaged wall-pressure and skin friction distributions are shown in Figure 5.1.2. The new models ('newest model' corresponds to the use of weighting method 1) give essentially identical results and provide a slight improvement over the Choi, et al. model in the prediction of the upstream extent of axial separation. Still, all models appear to over-predict the extent of separated flow – a fact further evidenced in the axial velocity profiles of Figure 5.1.3. The wake-like response encountered as the boundary layer moves over the low-momentum flow region at the corner is over-predicted by all models. This leads to a delayed recovery of the turbulent boundary layer downstream of re-attachment.

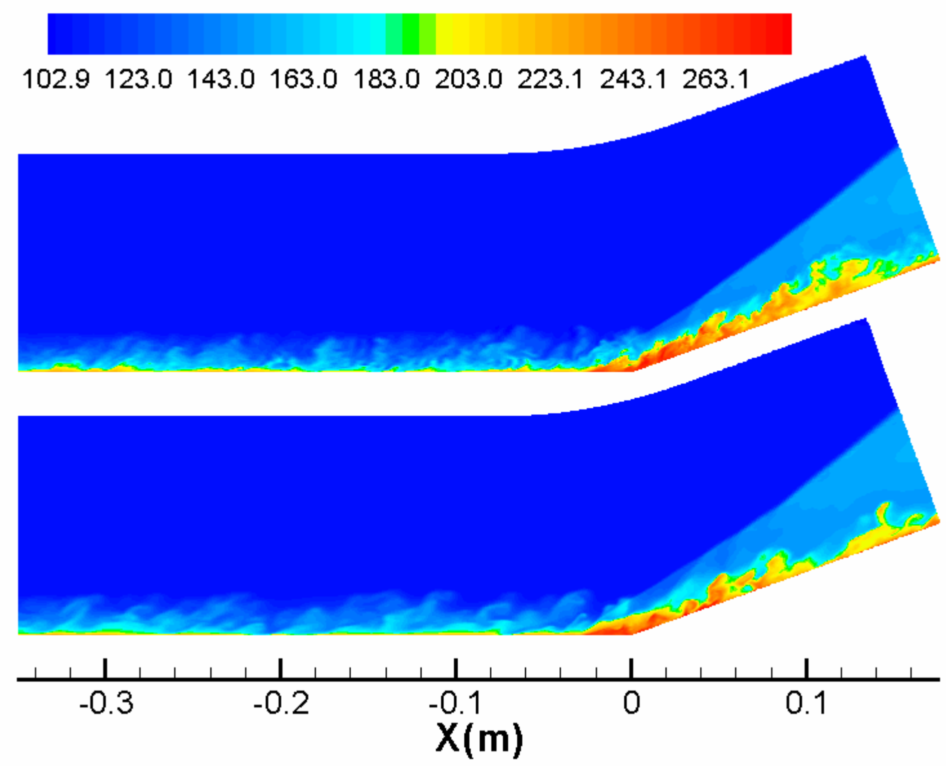

Figure 5.1.1: Centerplane temperature contours (top: LD-PPM, new model; bottom: PPM, model of Choi, et al.

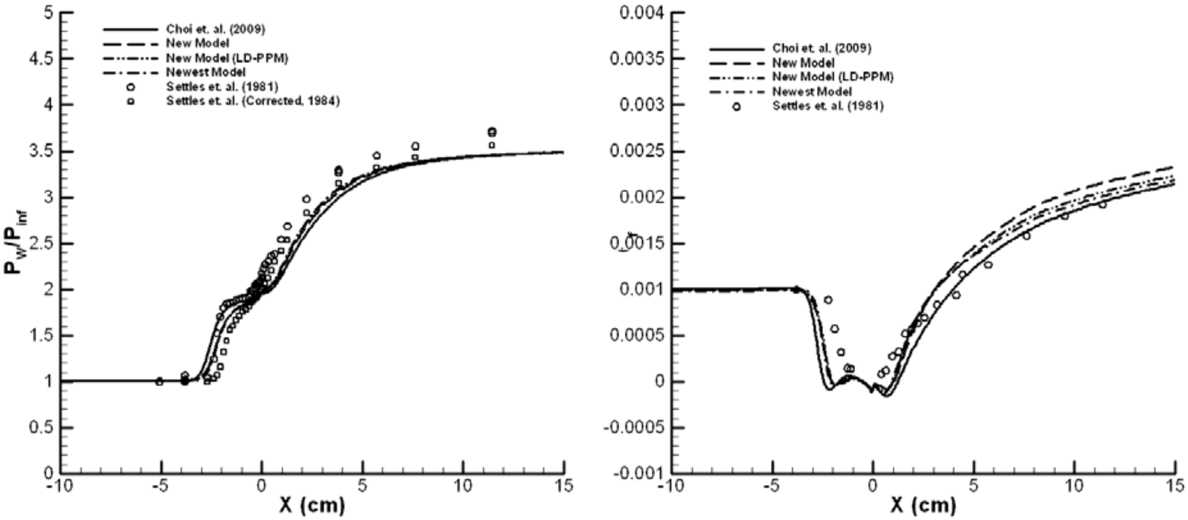

a.) b.)

Figure 5.1.2: Surface pressure and skin friction distributions: 20-degree compression corner

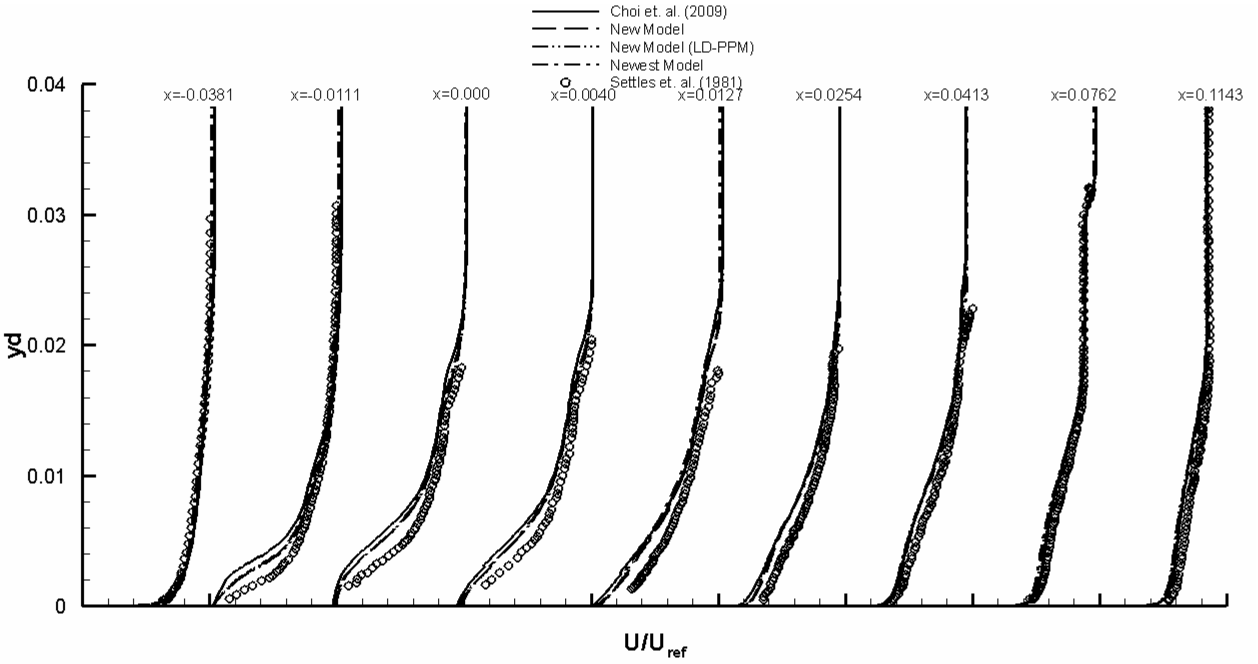

Figure 5.1.3: Velocity profiles throughout the interaction region

5.2. Reynolds stress predictions

Predictions of the *rms* mass flux fluctuation intensity and Reynolds stress fields, with the latter estimated both by Favre ensemble-averaging and by the use of Morkovin's strong Reynolds analogy (SRA) as utilized by Smits and Muck, are described in this section. Considering only the Reynolds axial and shear stresses, Favre-averaging yields

$$\bar{\rho}\overline{u_1'u_1'} = \overline{\rho u_1 u_1} - \frac{\overline{\rho u_1}\,\overline{\rho u_1}}{\bar{\rho}} \text{ (Reynolds axial stress)} \qquad (5.2.1)$$

and

$$\bar{\rho}\overline{u_1'u_2'} = \overline{\rho u_1 u_2} - \frac{\overline{\rho u_1}\,\overline{\rho u_2}}{\bar{\rho}} \text{ (Reynolds shear stress)} \qquad (5.2.2)$$

Morkovin's SRA requires first an expression for the rms mass flux fluctuation intensity:

$$\left(\overline{[(\rho u_1)']^2}\right)^{1/2} = [\overline{(\rho u_1)^2} - \overline{\rho u_1}\,\overline{\rho u_1}]^{1/2} \qquad (5.2.3)$$

from which

$$\bar{\rho}\overline{u_1'u_1'} = \frac{1}{\beta^2}\frac{\overline{[(\rho u_1)']^2}}{\bar{\rho}} \text{ (Reynolds axial stress)} \qquad (5.2.4)$$

and

$$\bar{\rho}\overline{u_1'u_2'} = \frac{1}{\beta}\overline{(\rho u_1)'u_2'} \quad \text{(Reynolds shear stress)} \qquad (5.2.5)$$

can be obtained. Here, $\beta^2 = 1 - 2R_{uT}(\gamma - 1)M_1{}^2 + [(\gamma - 1)M_1{}^2]^2$, with M_1 being the local average Mach number evaluated as u_1 / c, where c is the local sound speed, and R_{uT} is the correlation coefficient $\overline{u_1'T'}\Big/\left(\overline{(u_1')^2}\right)^{1/2}\left(\overline{(T')^2}\right)^{1/2}$, which is set to -0.8. Figure 5.2.1 shows the evolution of the rms mass fluctuation intensity throughout the interaction, while Figure 5.2.2 shows the evolution of the Reynolds axial and shear stress distributions. The Reynolds axial stress is most in error in the low-momentum region located near the wall downstream of re-attachment. Morkovin's SRA provides predictions that are close to those provided by Favre-averaging, and the fact that the rms fluctuation intensity is actually over-predicted by the LES/RANS methods means that the most probable cause of the discrepancy is an over-prediction of the vertical extent of the low-momentum region, as the average density and β^2 would both be lower than in the experiment. The Reynolds-shear stress predictions are off by at least a factor of two, but the uncertainty in the experimental measurements due to probe misalignment and calibration errors is believed to be very high.

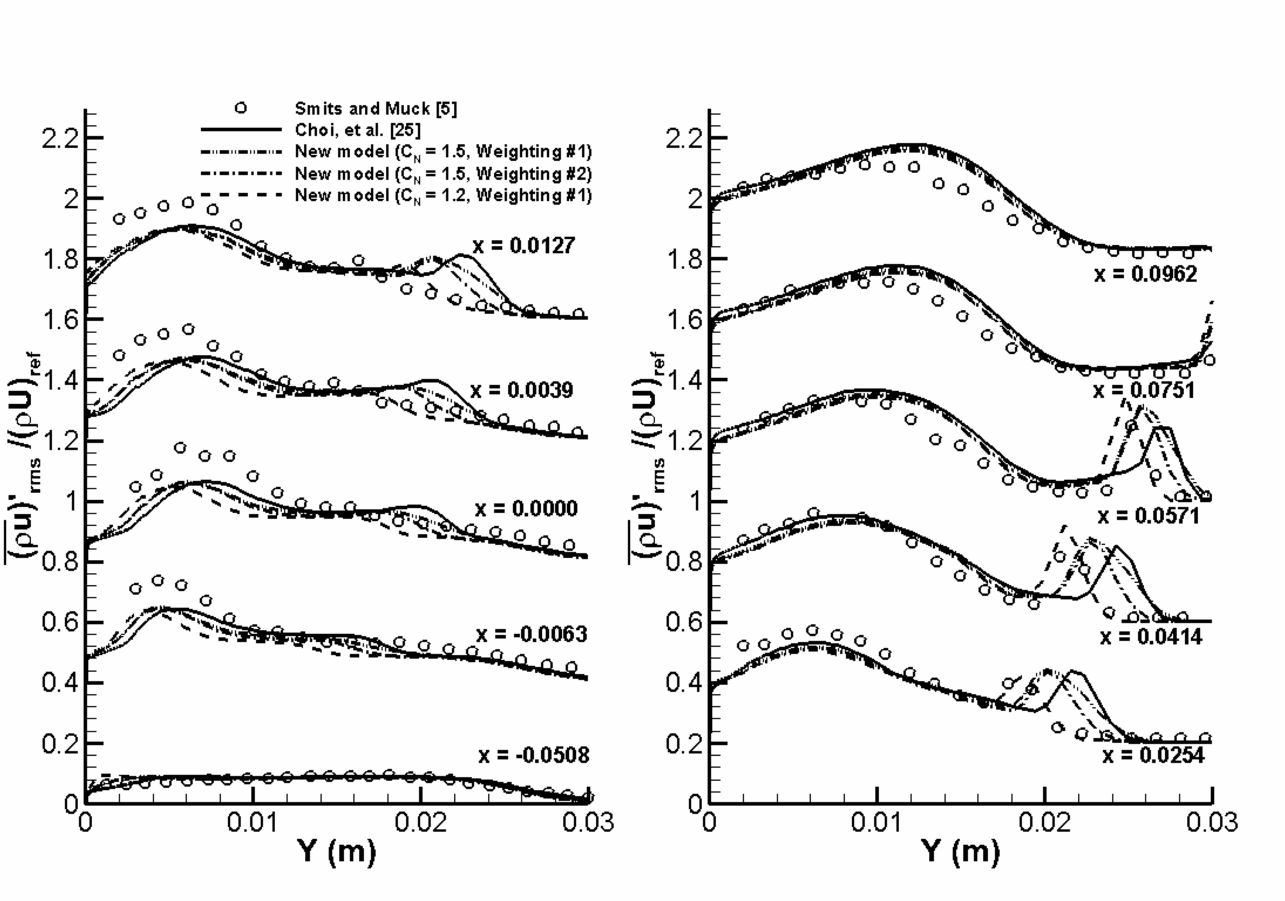

Figure 5.2.1: Mass flux fluctuation intensity distributions

5.3. Shock motion: 20 degree interaction

We have used several sampling techniques to study aspects of separation-shock motion for the 20-degree interaction. There appear to be two distinct responses present, both of which can influence the observed intermittency characteristics in this flow. As shown in Figure 5.3.1, streak-like structures present in the incoming boundary layer can disturb the shock front, pushing it upstream and downstream of its time-averaged position. The extent of shock motion can be quantified by an intermittency distribution, defined as the amount of time that the shock is

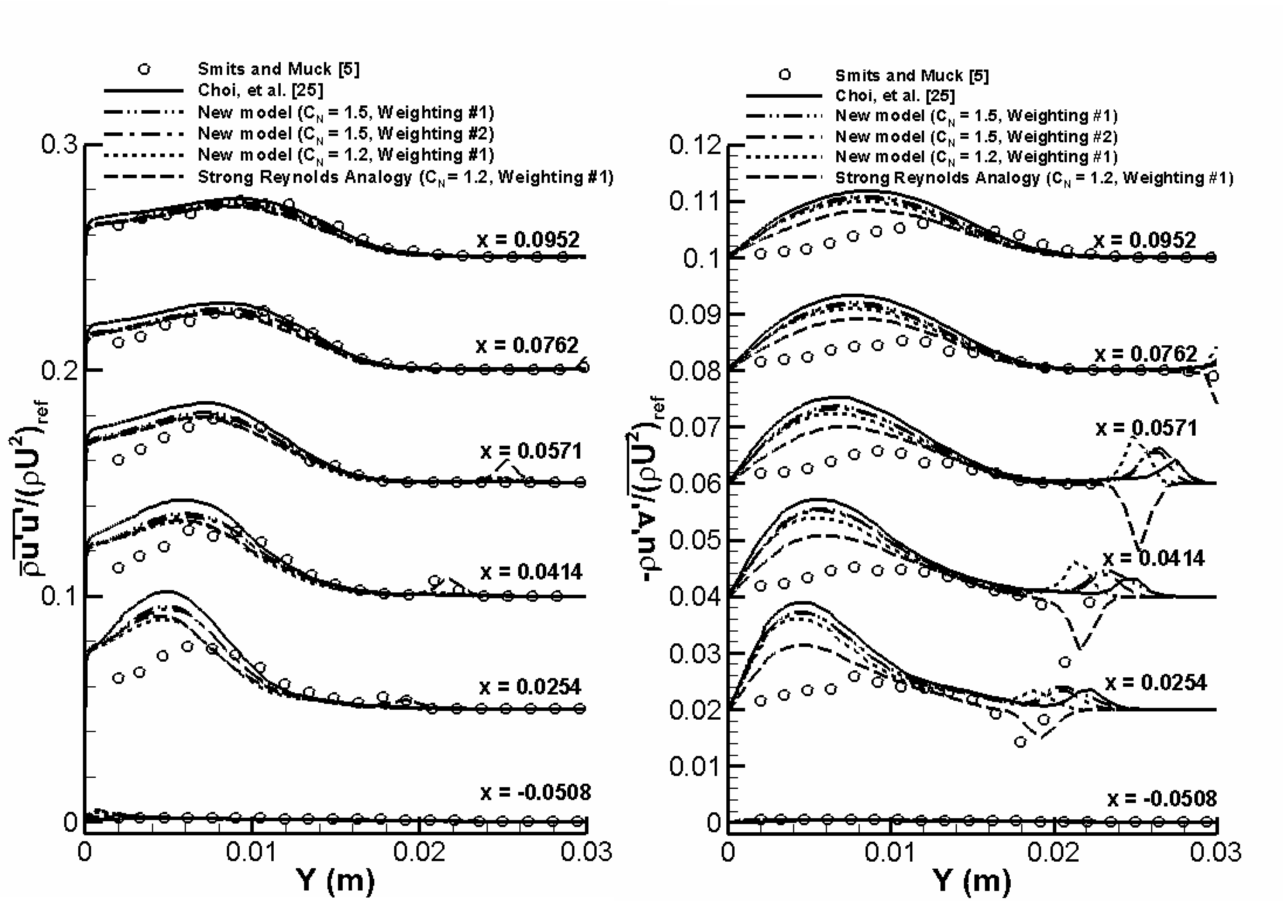

Figure 5.2.2: Reynolds axial stress (left) and shear stress (right) distributions

upstream of a particular location. This is shown in Figure 5.3.2 for the 20-degree interaction. The shock front moves over a range of ~0.6 boundary layer thicknesses. A low-frequency signal

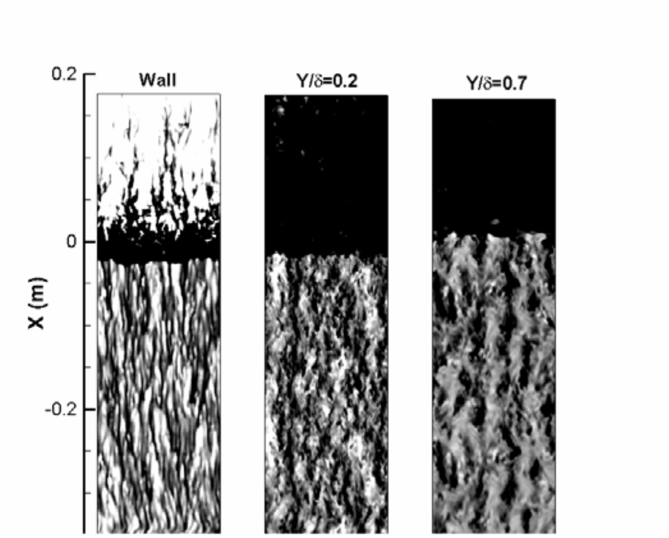

Figure 5.3.1: Velocity magnitude contours at different wall-normal planes

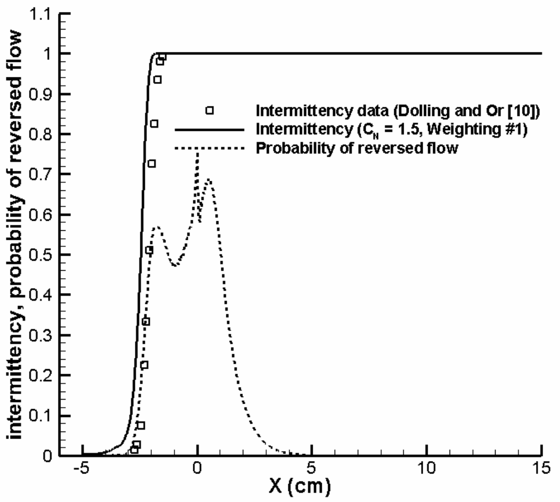

Figure 5.3.2: Intermittency and probability of reversed-flow distributions.

is also observed, as indicated in the spectral maps shown in Figure 5.3.3. Here, the normalized power spectrum is plotted at different X stations throughout the interaction. A shift to a lower-frequency band is noted near the separation shock position, followed by a recovery toward a typical boundary layer spectrum as the flow re-attaches on the compression ramp. Also noted in Figure 5.3.3 are two estimates for the dominant low-frequency signal, one from the correlation of Dupont [14]:

$$S_L = \frac{f_{sh} L_{sep}}{U_\infty}, S_L = 0.025, \qquad (5.3.1)$$

and another from a residence-time distribution analysis to be discussed later. Both estimates are in close agreement with the observed peak in the low-frequency signal.

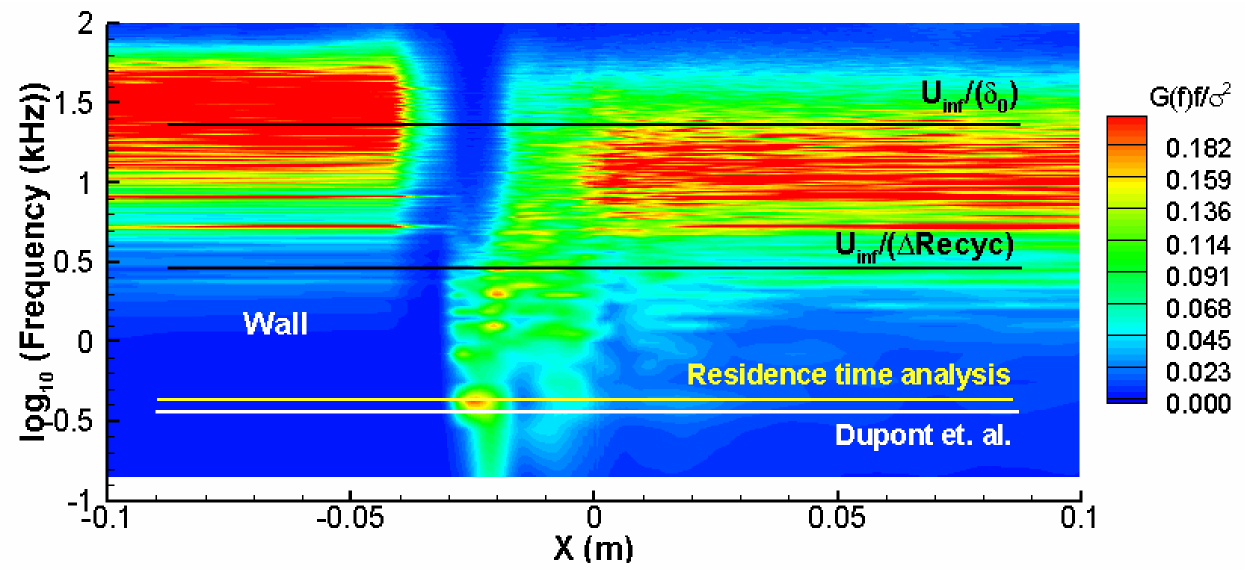

Figure 5.3.3: Spectral maps extracted at different Y locations – 20-degree interaction.

6. Model Assessment: 24-degree Sharp Compression Ramp

6.1. Mean flow behavior

Here, we repeat many of the analyses performed for the 20-degree interaction for the case of nominal Mach 3 flow over a 24 degree compression corner. [13] The shock wave in this case is strong enough to induce a large region of separated flow – extending ~6 cm upstream of the wedge apex. Figures 6.1.1 and 6.1.2 present surface pressure and skin friction distributions, respectively. As noted, all LES/RANS models over-predict the upstream extent of flow separation for this case. The newer models, perform better in this regard, and there is little difference in the predictions with respect to the choice of the ensemble-averaging technique. Figure 6.1.3 shows velocity profiles extracted throughout the interaction. These also indicate an over-prediction of the size of the backflow region and an associated delay in the boundary-layer recovery rate.

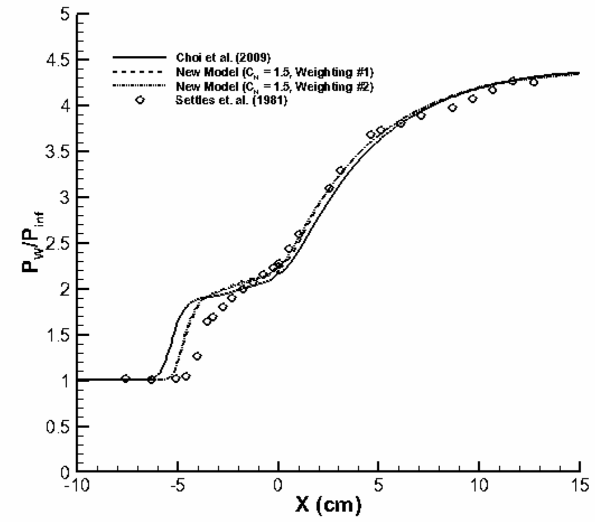

Figure 6.1.1: Surface pressure distributions

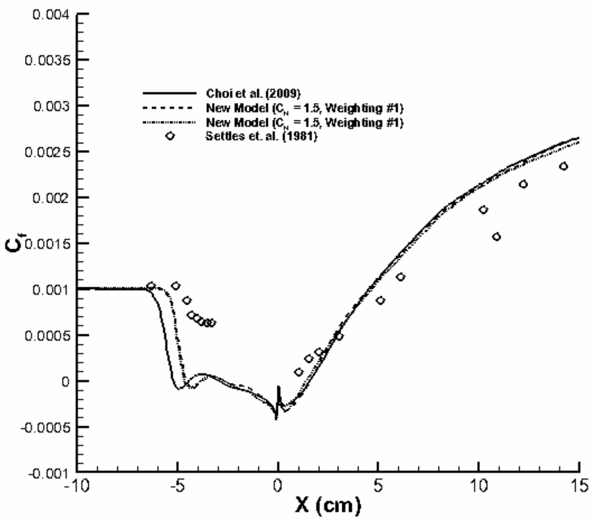

Figure 6.1.2: Surface skin friction distributions

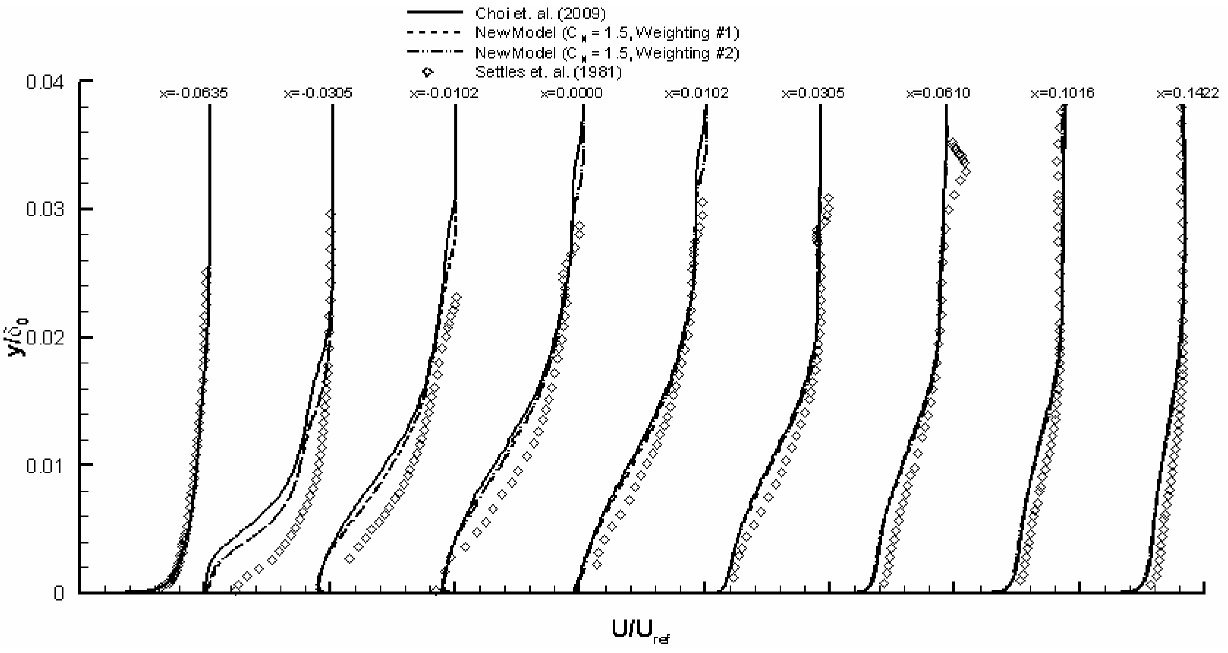

Figure 6.1.3: Velocity profiles throughout the interaction region

6.2. Reynolds stress predictions.

As in the 20-degree interaction, we have extracted Reynolds stress statistics using Favre ensemble averaging and using Morkovin's strong Reynolds analogy. Predictions of *rms* mass flux fluctuation intensity in Figure 6.2.1 show good agreement with the peak values and their

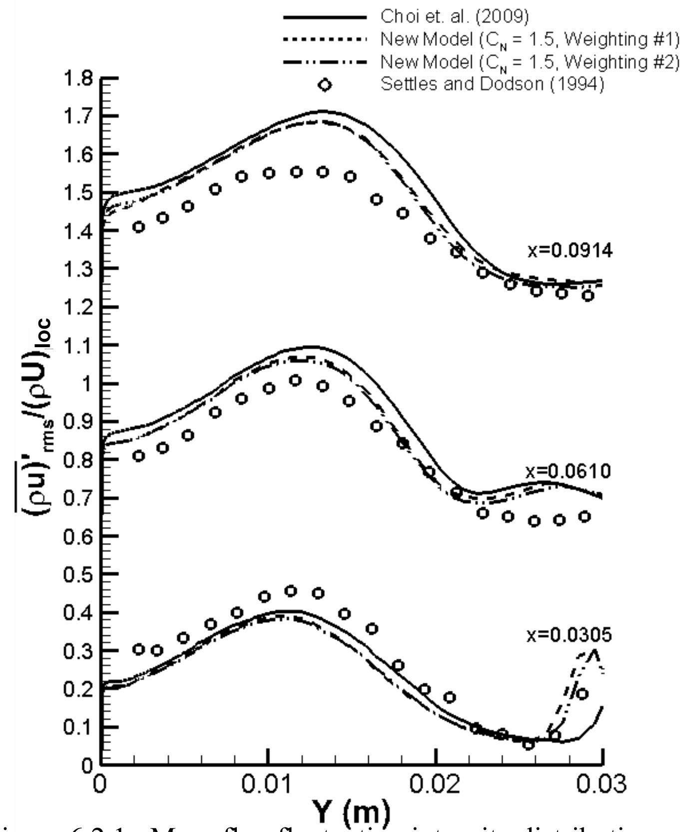

Figure 6.2.1: Mass-flux fluctuation intensity distributions

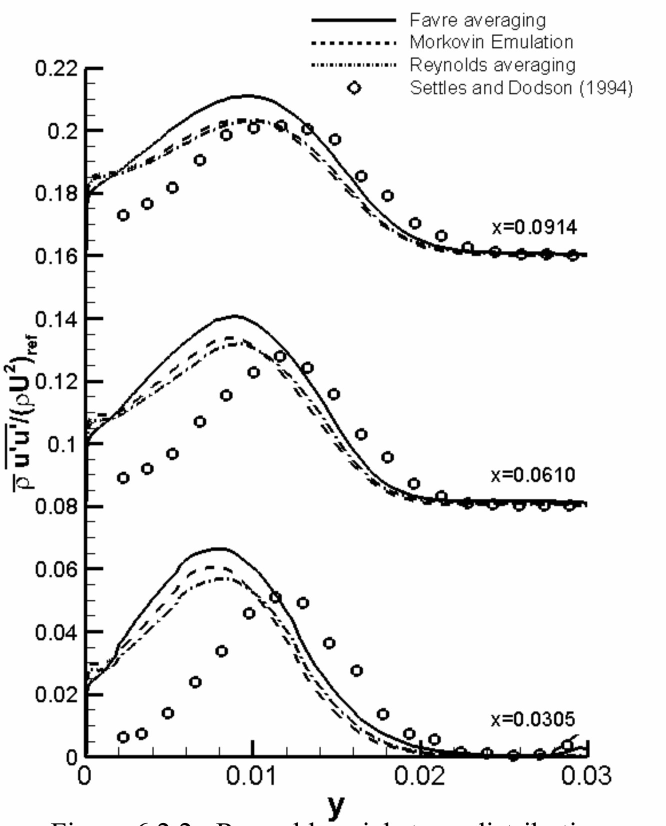

Figure 6.2.2: Reynolds axial stress distributions (strong Reynolds analogy)

locations, but this is somewhat misleading, as the intensity curves are normalized with respect to the mean momentum flux, which also is in error due to the separation prediction being incorrect. As such, the Reynolds axial stress distributions (Figure 6.2.2) show significant discrepancies, and the use of Morkovin's SRA provides no real improvement. These results provide more evidence that inaccuracies in the prediction of the structure of the backflow region affect the

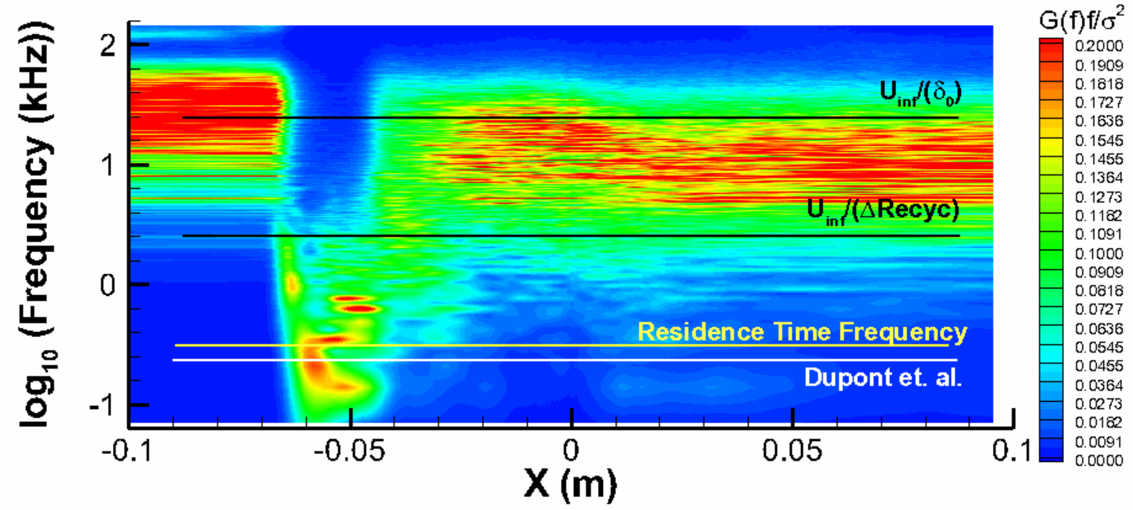

Figure 6.3.1: Power spectra distributions: 24-degree ramp

entirety of the downstream flow.

6.3. Shock motion – 24 degree interaction and residence time analysis

We have also extracted wall pressure spectra for the 24 deg. case, and as expected, it also shows a shift to lower frequencies in the vicinity of the separation shock. Figure 6.3.1 shows wall pressure spectra for the 24-degree ramp. A larger region of low-frequency motion is indicated upstream of the compression ramp, indicating that the response scales with the size of the separation region.

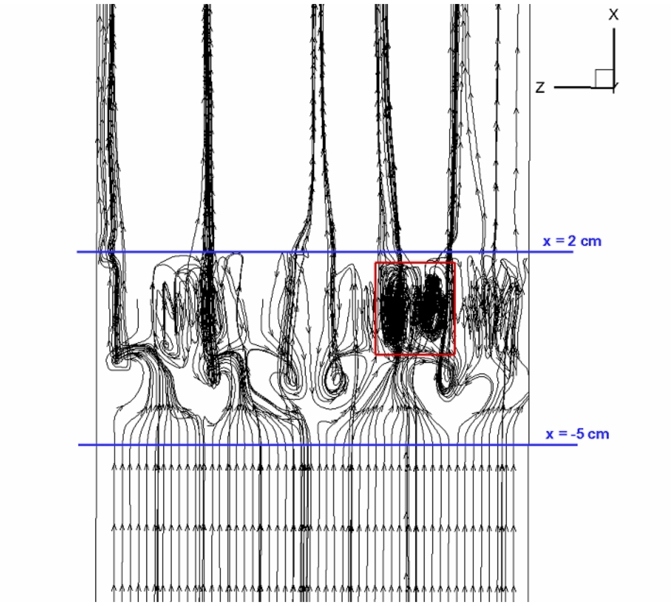

Figure 6.3.2: Streamlines entering separation region (view from above, 24-degree interaction)

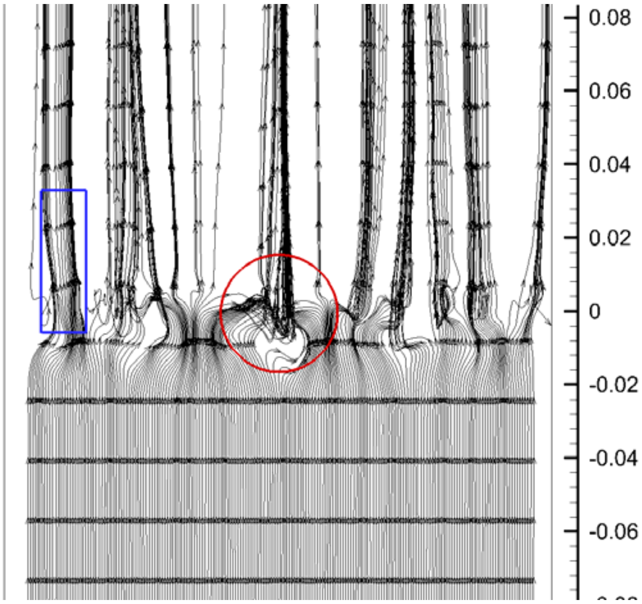

Figure 6.3.3: Streamlines entering separation region (view from above, 20-degree interaction)

The lines corresponding to “Residence time analysis” and “Residence Time Frequency” in the above figures are from a new analysis that extracts residence-time distributions for fluid particles entering the recirculation zones. The fact that a large amount of experimental data can be collapsed into a relatively narrow range of Strouhal numbers according to Dupont’s correlation [14] suggests that the dominant time scale must be one associated with entrainment of fluid into and out of the recirculation region, which naturally would scale with the length of the separation region. To explore this, a collection of 4000 evenly-distributed streamlines passing through the separation region were analyzed to determine the amount of time a fluid particle would spend in this region. To do this, a line integral of velocity magnitude was performed along each streamline, starting when the streamline crossed x = -5 cm and ending once it had crossed x = 2 cm. Figure 6.3.2 shows a top view of an ensemble of near-surface streamlines for the 24-degree interactions, while Figure 6.3.3 shows the same for the 20-degree interaction. A weakly-separated flow, characterized by significant spanwise migration of fluid particles and complex topological features, is found in the region of intermittent separation-shock motion. Further downstream, a more ‘two-dimensional’ separation pattern is found at intervals in the spanwise (Z) direction. The blue lines in Figure 6.3.2 indicate the X stations where integration begins and ends. The red rectangle highlights streamlines within one of the ‘two-dimensional’ sections of the separated region, where the vorticity vector points predominately in the Z direction.

Once the times were calculated for each streamline, a probability density function for the residence time distribution was created, as shown in Figure 6.3.4. The most probable residence time is 3.23e-3 seconds for the 24-degree interaction and 2.25e-3 for the 20-degree interaction. The frequencies associated with these residence times are close to the shock motion frequencies predicted for this case by the Dupont et al. correlation and coincide with one of the local peaks in the spectral map. These results provide evidence of a connection between the observed low-frequency signal and the time required for fluid to enter and leave the recirculation zone. The fact that residence time distributions of this type can be obtained from mean-flow data indicates that it might be possible to predict a dominant low-frequency model without conducting an unsteady analysis. The challenge is in identifying entrainment pathways so that an appropriate sampling window can be constructed.

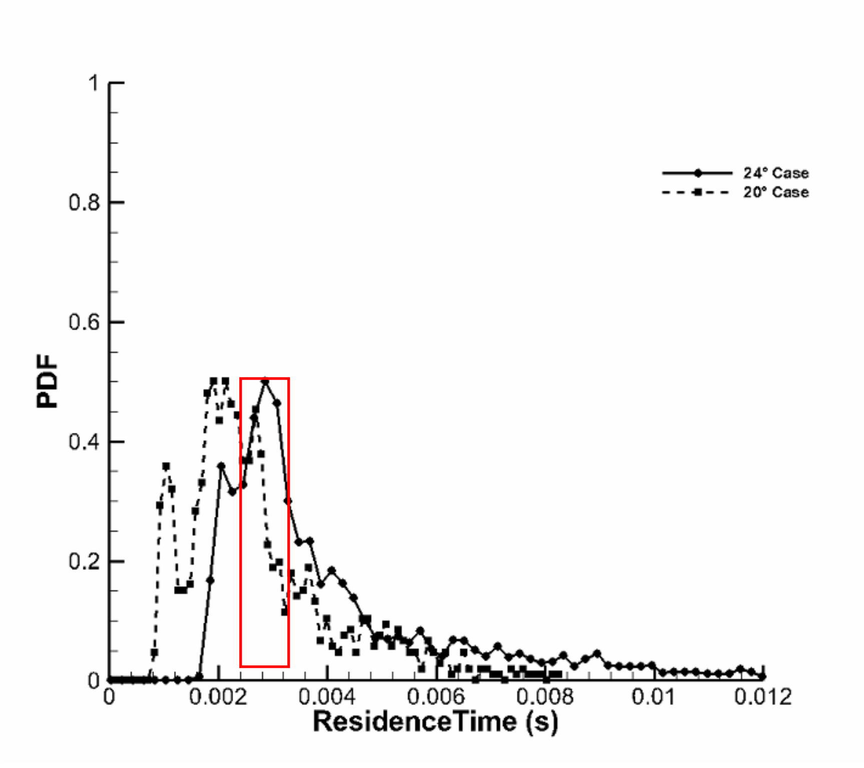

Figure 6.3.4: Residence time distributions (20-degree and 24-degree ramps

7. Model Assessment: 3D Shock / Boundary Layer Interaction

We have conducted LES/RANS simulations of a Mach 2.5 shock / boundary layer interaction in a wind tunnel (experiments conducted at Cambridge University [15]) as a means of assessing methods described in Section 2.3 for maintaining a RANS-type response in regions of the flow that are not resolved enough to sustain turbulence. The shock is generated by an 8-degree compression ramp placed on the top of the wind tunnel. The shock impinges upon the bottom surface of the wind tunnel, creating a region of shock-separated flow. The structure of the SBLI is known to be impacted by corner vortices that are generated through interactions between the oblique shock and the sidewall boundary layers. These force fluid toward the corner, reducing the effective cross-sectional area of the wind tunnel and causing the core flow to accelerate around the displaced viscous layer. The mesh contains about 46 M cells but is not refined significantly in the Y direction, rendering it unsuitable for sustaining turbulence in the sidewall boundary layers. Figure 7.1.1 shows a center-plane snapshot of temperature, illustrating the fact that turbulence is sustained in the top and bottom surface boundary layers. Thickening of the boundary layer due to shock impingement is also indicated. The impact of corner vortices on the near-surface flow field is illustrated in Figure 7.1.2, a plot of near-surface streamlines colored by axial velocity magnitude. The left figure corresponds to the use of the 'RANS wall' option, while the right figure corresponds to the use of grid-scale limiting (see Section 2.3) The predictions are similar, indicating that the structure of the corner vortices is not significantly impacted by this choice.

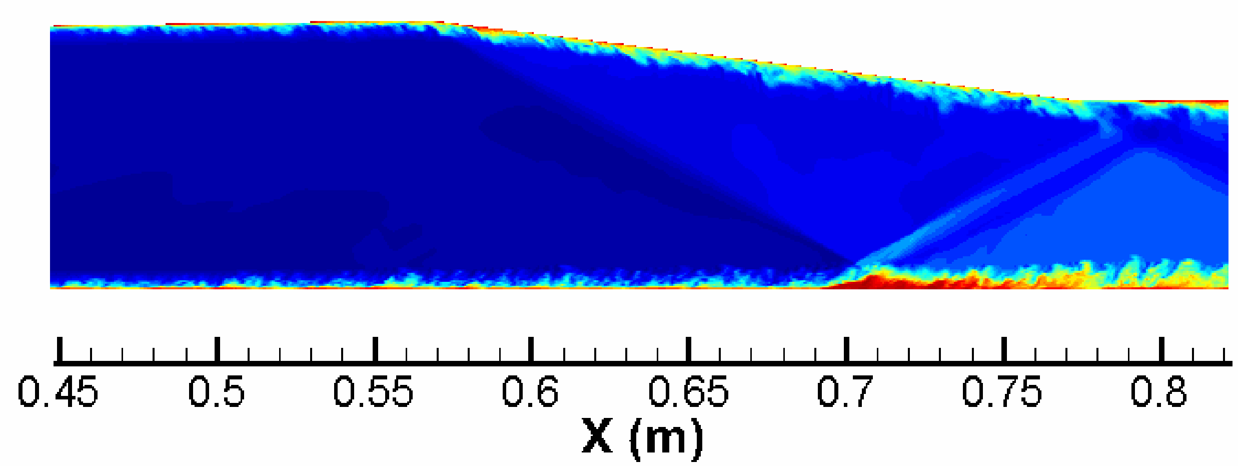

Figure 7.1.1: Centerplane temperature contours: Cambridge SBLI

The effect of both techniques in attenuating resolved-scale turbulence is illustrated in Figure 7.1.3, which plots instantaneous temperature (bottom) and eddy viscosity (top) contours at the shock crossing location. The grid-scale limiting method is somewhat less aggressive, as it produces smaller eddy viscosities and does allow some turbulence content to remain in regions near the corners.

Centerline velocity profiles within the interaction and centerline surface pressure distributions are shown in Figure 7.1.4. These indicate that the LES/RANS method performs very well in capturing the response of the viscous layer to the shock wave.

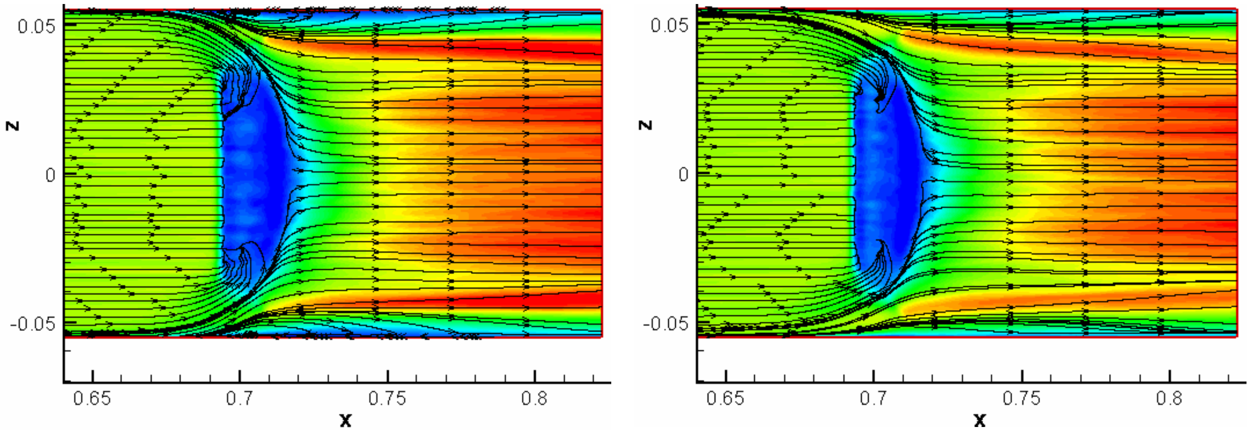

Figure 7.1.2: Near-wall flow structure for Cambridge SBLI (left: 'RANS wall'; right: grid-scale limiting)

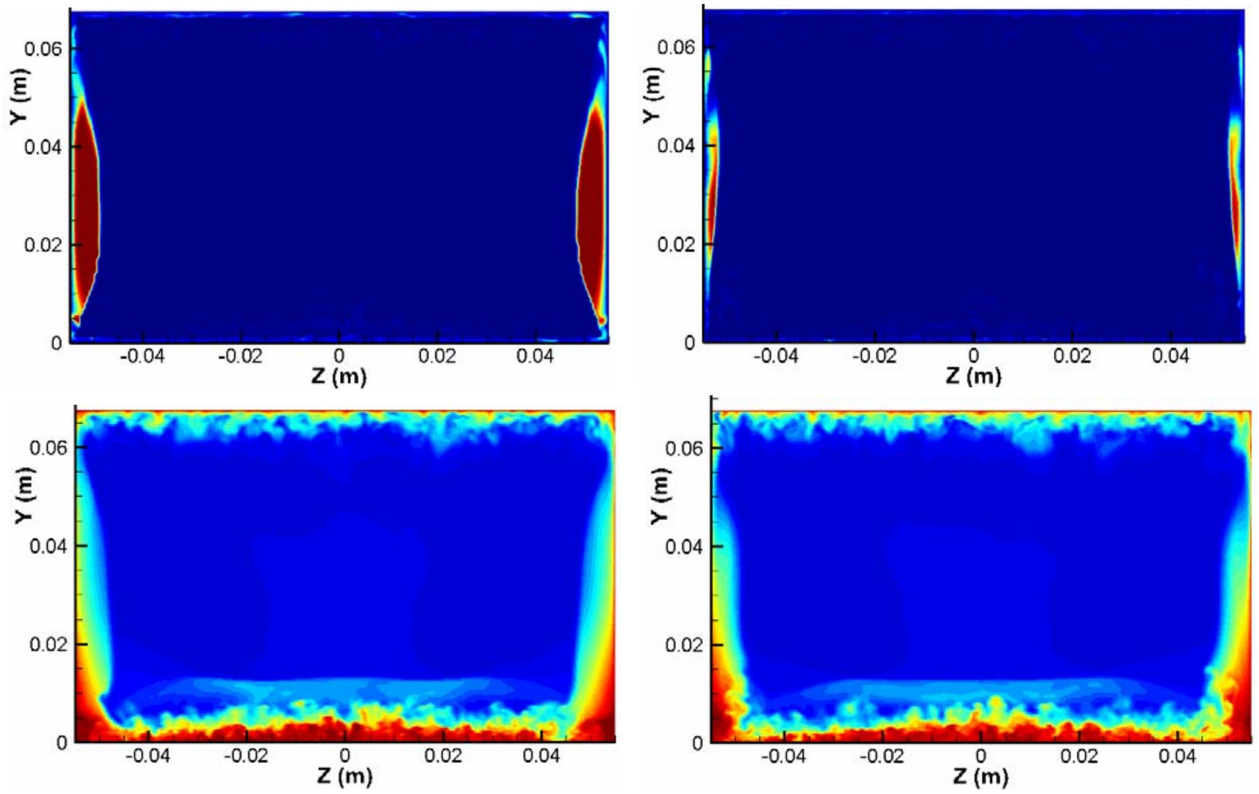

Figure 7.1.3: Eddy viscosity (top) and temperature (bottom) contours at shock-crossing location (left: 'RANS wall'; right: grid-scale limiting)

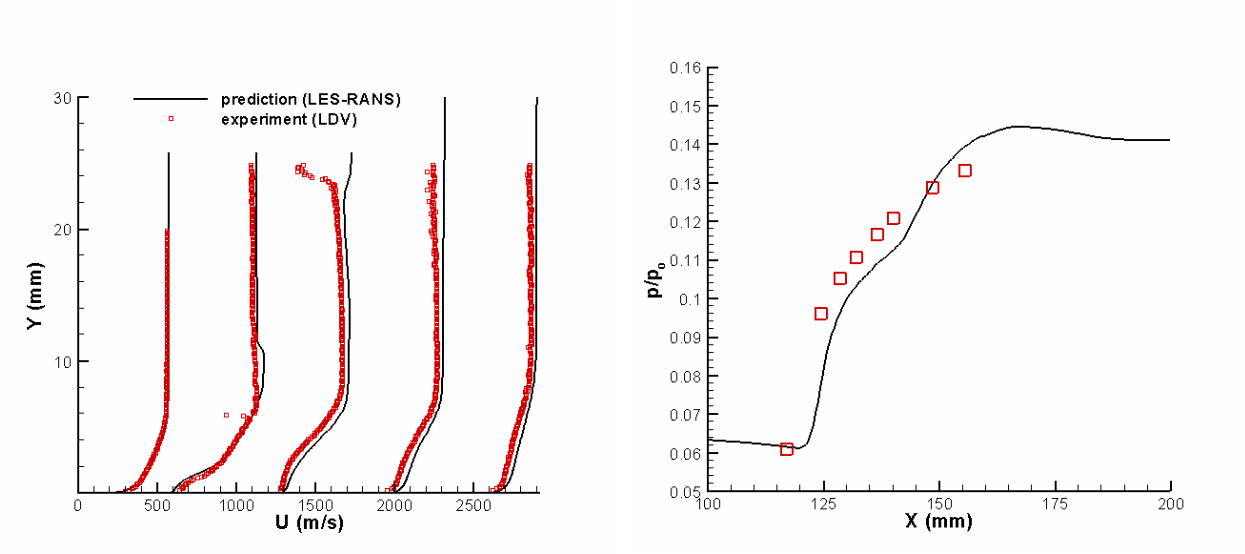

Figure 7.1.4: Centerline velocity profiles (left) and surface pressure distribution (right): Cambridge SBLI

8. Model Assessment: Airfoil near Static Stall

It is of interest to investigate the performance of the LES/RANS model for low-speed flows characteristic of helicopter aerodynamics, as there is a significant interest within ARO in better prediction methods for dynamic stall. In our past work, we have used recycling / rescaling techniques to sustain turbulence within boundary layers. These will not generally work for airfoil-type flows, as they rely on a RANS base state and as airfoil turbulent boundary layers will be initiated by growth of natural instabilities within a laminar boundary layer or within a laminar separation region. It is of interest, therefore, to determine the baseline response of the current LES/RANS methods for flow over an airfoil. To this end, we have conducted a simulation of flow over an 'A-Airfoil' (an Aerospatiale design) at conditions near static stall [16]. Mary and Sagaut [17] previously conducted a large-eddy simulation of this flow. The free-stream Mach

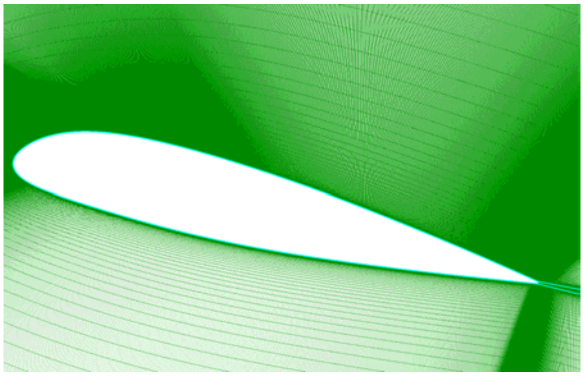

Figure 8.1.1: X-Y centerplane mesh for A-airfoil

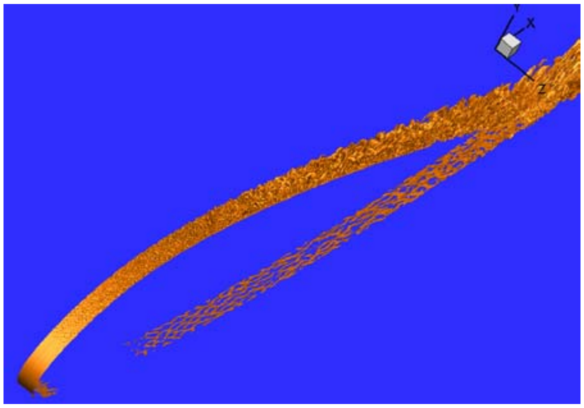

Figure 8.1.2: Iso-surfaces of swirl strength (2000 s^{-1}) illustrating development of eddy structures in airfoil boundary layer

number is 0.15, the Reynolds number based on a chord length of 0.6 m is 2.1e6, and the angle of attack is 13.3 degrees. An X-Y snapshot of the computational mesh, which contains ~30e6 cells, is shown in Figure 8.1.1, and an iso-surface of swirl-strength, illustrating the growth of large turbulent eddies on the suction side, is shown in Figure 8.1.2. Comparisons with experimental velocity profile data (Figure 8.1.3) and turbulence intensity data (Figure 8.1.4) are generally favorable, though the turbulence intensity level is under-predicted near the trailing edge, an effect also observed by Mary and Sagaut [16]. The first model tested (Choi, et al. [2] requires a pre-selection of a model constant that varies with chord along the upper and lower surfaces. The

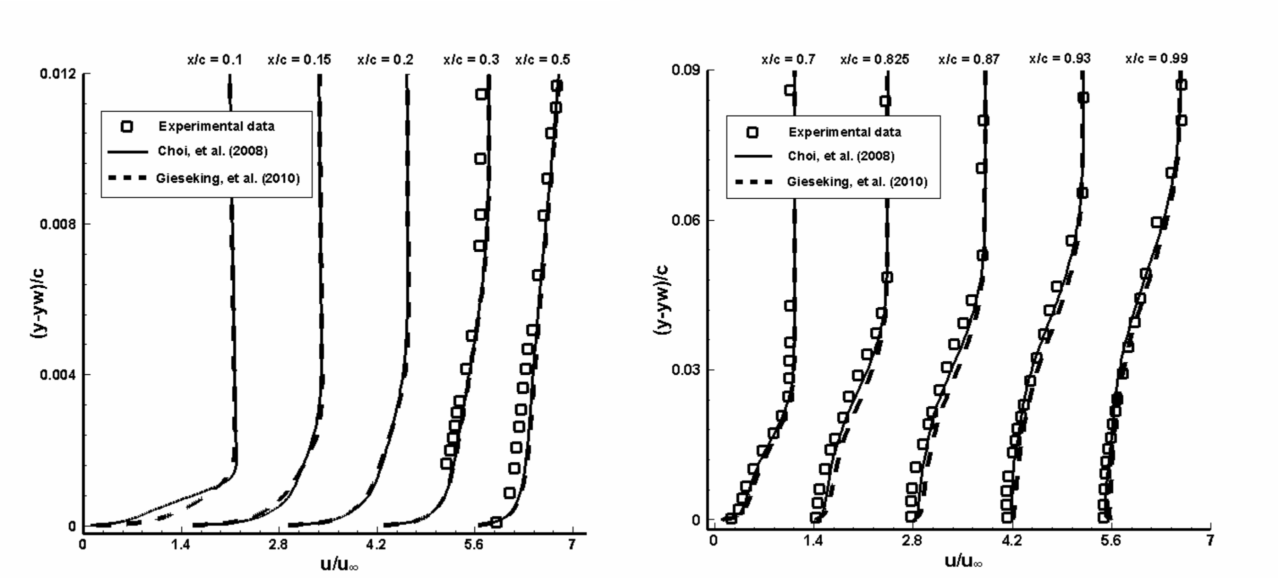

Figure 8.1.3: Streamwise velocity profiles along airfoil surface.

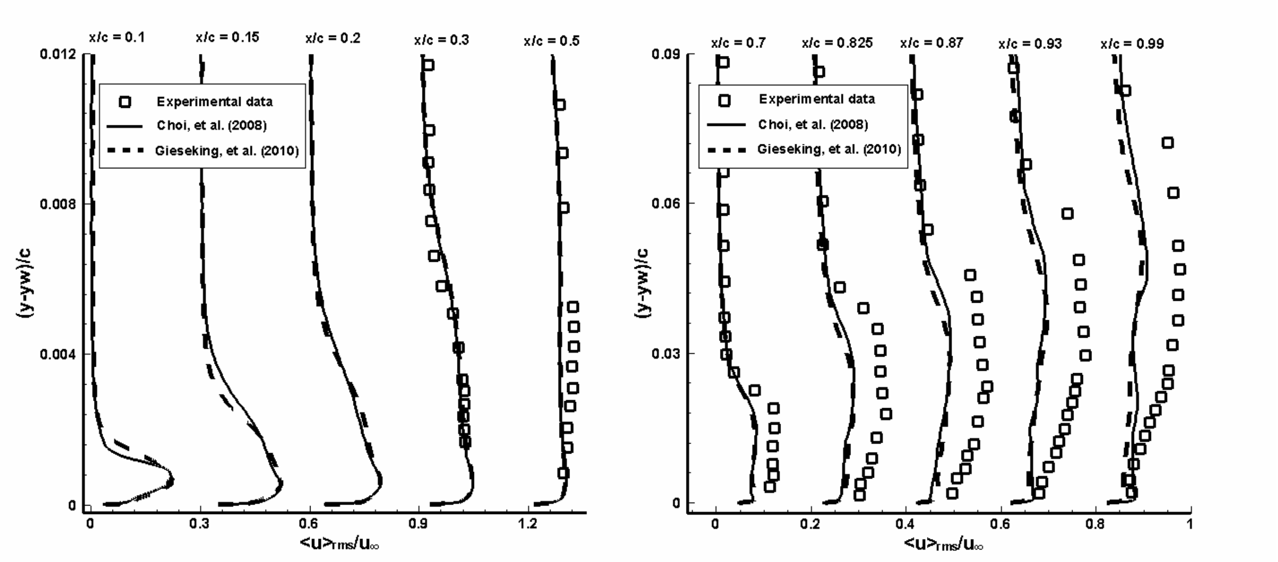

Figure 8.1.4: Streamwise *rms* velocity fluctuation profiles along airfoil surface

calculation of this quantity, described in detail in [2], requires an estimate of the boundary layer edge and the flow properties at that edge. This information was obtained for the lower and upper airfoil surfaces from an initial RANS calculation. The new model, developed during this grant, does not need this information. Comparisons with surface pressure coefficient (Figure 8.1.5) and skin friction (Figure 8.1.6) distributions also show good agreement with experiment. However, the reference for the experiment [15] and the LES computations presented in [16] indicate that a laminar separation bubble should be present. Neither of the LES/RANS models predicts a region of laminar flow near the leading edge, indicating the need to include a transition model for the RANS component of this closure.

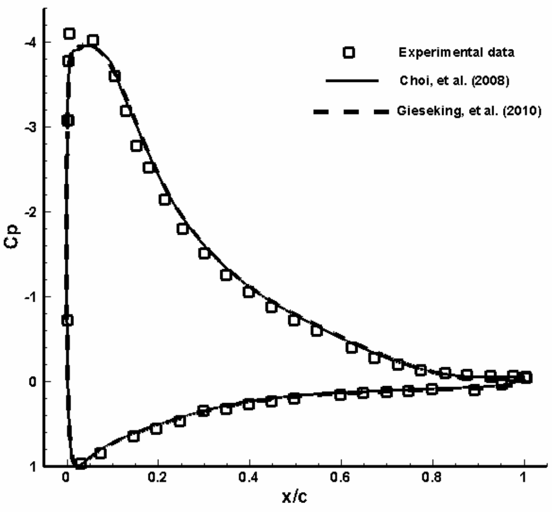

Figure 8.1.5: Surface pressure coefficient for Aerospatiale 'A-airfoil'

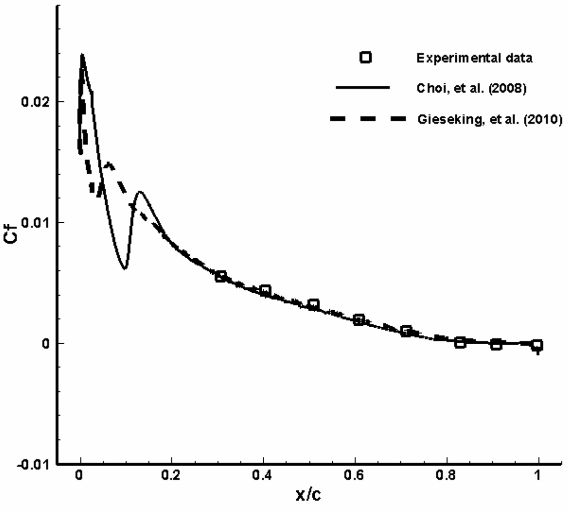

Figure 8.1.6: Surface skin friction coefficient for Aerospatiale 'A-airfoil'

9. Large-eddy Simulations of the Elena-Lacharme Flat-Plate Boundary Layer Experiment

Though the LES/RANS model works reasonably well, there are still aspects of the formulation that need improvement. Among these is the fact that accurate predictions of the mean boundary layer structure can only be accomplished at the expense of accurate predictions of the axial Reynolds stress, which can be important in shock / boundary layer interactions. It is clear that the shift from LES to RANS brings about a redistribution of Reynolds stresses that may not be correct. If the transition from RANS to LES is designed so that it occurs in the lower part of the logarithmic region, then the turbulence intensities may be well-predicted but the overall mean flow is accelerated more than it should be. This leads to the so-called 'log law mismatch', which plagues nearly every LES/RANS model.

A path forward to resolving this issue is to have a more 'exact' solution available for comparison. To this end, we have conducted wall-resolved large-eddy simulations and direct numerical simulations of the Elena and Lacharme [7] flat-plate boundary layer experiment. Resolution requirements for a wall-resolved LES are much more severe than for a RANS or LES/RANS, and the predictions are much more sensitive to the level of numerical dissipation employed and to the form of the selected subgrid model. It also was necessary to recycle both mean and fluctuating data, simply as there was no RANS base state upon which to super-impose recycled fluctuations. Several cases were run, as summarized in Table 9.1. The naming convention follows that used in the figures discussed next. In some cases, better resolution of the flow in the Z direction was expedited by reducing the Z extent of the domain while maintaining a constant cell count. This turned out to be a bad idea, as it also reduced the thickness of the boundary layer and made some results difficult to interpret. The baseline numerical scheme used was the LD-PPM (low dissipation piecewise parabolic method) developed in Year 1 of the grant. This scheme uses the Ducros, et al. vorticity / divergence switching function to shift the inviscid flux discretization from PPM in shock-dominated or free-stream regions (switch = 1) to a fourth-order central scheme in vorticity-dominated regions (switch = 0). The specific switch includes a thresholding constant that can maintain some of the PPM contribution even when the Ducros switch is nominally zero. While we have used this routinely in LES/RANS applications, it is necessary to set this constant to zero for LES/DNS applications, as otherwise, too much numerical dissipation can corrupt the solution. The nomenclature '-NT' refers to setting this thresholding constant (called 'cutoff' in the Table) to zero.

Table 9,1: Cases run for LES/DNS studies

Case	cells in X/δ	cells in Z/δ	SGS	cutoff	discretization
DNS	30	30	none	0.1	LD-PPM
DNS-NT	30	30	none	0.0	LD-PPM
DNS-PPM	30	30	none	N/A	PPM
DNS-1/2 dz	30	60	none	0.0	LD-PPM
DNS fine	40	60	none	0.0	LD-PPM
LES-NT	30	30	Lenormand	0.0	LD-PPM
LES-NT-smag	30	30	Leveque	0.0	LD-PPM
LES-NT-2/3 dz	30	45	Lenormand	0.0	LD-PPM
LES-NT-1/2 dz	30	60	Lenormand	0.0	LD-PPM
RANS	30	30	N/A		TVD

Nomenclature: DNS = direct numerical simulation; LES = large-eddy simulation, LD-PPM = low-dissipation piecewise parabolic method, TVD = total variation diminishing, cutoff = thresholding parameter in LD-PPM, dz = grid spacing in Z direction, SGS = subgrid-scale closure, δ = boundary layer thickness; X = streamwise direction, Z = spanwise direction

Figure 9.1.1 shows boundary-layer momentum thickness (left) and skin friction (right). The values of the momentum thickness are smaller for the cases that decreased the effective mesh spacing in the Z direction by reducing the spanwise extent of the domain. In effect, the solution 'converged' to a thinner boundary layer than anticipated. Because both the mean flow and the fluctuation fields are rescaled and recycled, there is no direct way to constrain the inflow boundary layer thickness. None of the LES or DNS solutions predict as high of a skin friction coefficient as does the RANS model, but as the boundary layer becomes thinner, the values increase. The Lenormand SGS model yields a higher skin friction level than the Leveque, et al. [10] modified Smagorinsky model for the same mesh. Reducing the cutoff parameter from 0.1 to zero also promotes an increase in skin friction, and the use of the PPM method alone reduces the skin friction greatly, implying that this scheme leads to excessive dissipation of the near-wall eddy structures. The skin friction distributions also show that there is an 'adjustment' period of about four boundary layer thicknesses for the LES or DNS solutions before the correct trends begin to emerge.

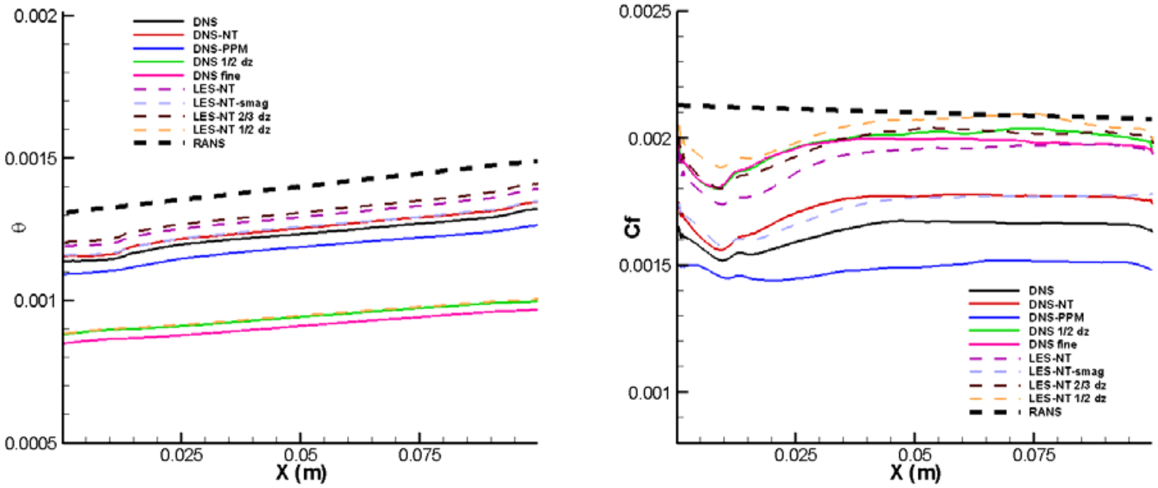

Figure 9.1.1: Momentum thickness (left) and skin friction (right) versus streamwise distance

Figure 9.1.2 plots the velocity profile in wall coordinates (left) (note that the axes are labeled incorrectly) and in a modified way in which the velocity is normalized by the free-stream velocity and the wall distance is normalized by the boundary layer thickness (right) but a logarithmic scale is still used. The second way reduces the influence of the general under-prediction in skin friction noted in Figure 9.1.1. Also shown in the right figure as dashed lines is the eddy viscosity (dimensional units) for each of the LES cases.

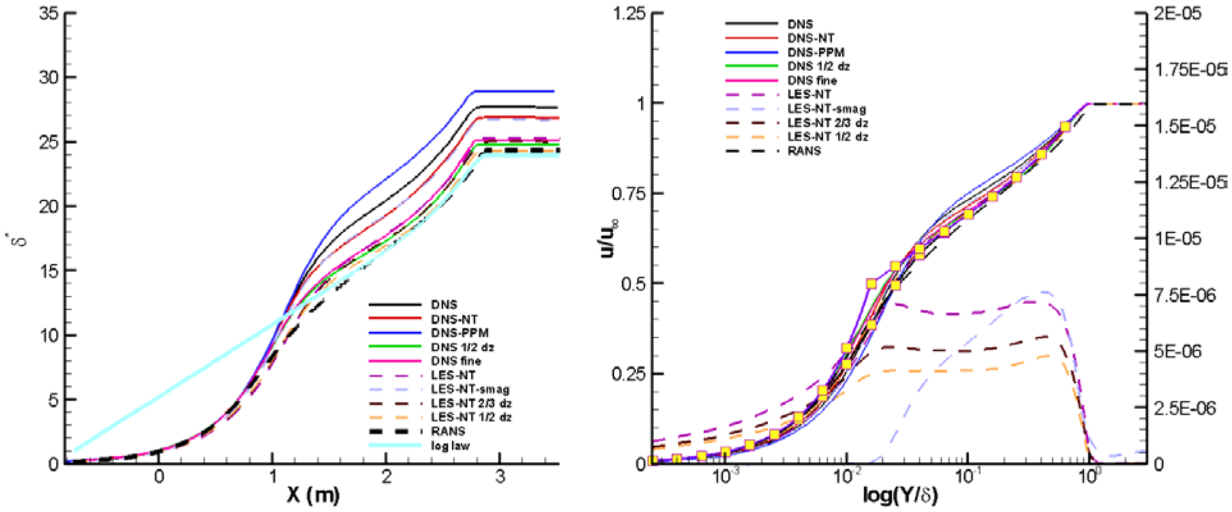

Figure 9.1.2: Velocity profile in wall coordinates (left) and in outer-layer coordinates (right)

There are several points to note. First, in the left figure, the predictions improve, relative to the theoretical wall / wake law, as the skin friction prediction improves. The LES and DNS predictions consistently rise over the wall / wake law in the buffer region, while the RANS prediction lies below the theory. The right figure also includes Coles' law of the wall / wake, transformed into outer-layer coordinates as yellow dots. Two such plots are shown – one which includes a hyperbolic-tangent blending of the viscous sub-layer solution with the logarithmic solution and one that does not. The use of outer-layer scaling collapses the predictions better. This figure clearly shows that the DNS calculations with LD-PPM and a zero cutoff and the LES calculations with LD-PPM, a zero cutoff, and the Lenormand subgrid-scale model provide the best results in the logarithmic and wake regions. The Leveque, et al. modified Smagorinsky model fares poorly but does lead to nearly vanishing eddy viscosity in the laminar sub-layer. In contrast, the Lenormand, et al. SGS viscosity does not decay as rapidly in the buffer layer and as a possible consequence, this model under-predicts the velocity in the laminar sub-layer. Calculations approach theory for this model as the mesh spacing in the Z direction is reduced. The RANS and LES/DNS predictions in the buffer layer are different and it is not clear which one is correct.

Predictions of Reynolds shear stress and mean velocity (left) and *rms* axial and normal fluctuation velocities (right) are shown in Figure 9.1.3 in outer-layer coordinates. Note that the X-axis of the right figure should also be Y/δ. The actual boundary layer thickness as predicted by each model is used in the normalization; this reduces the scatter in the predictions for the Reynolds shear stress and velocity but not for the *rms* velocities.

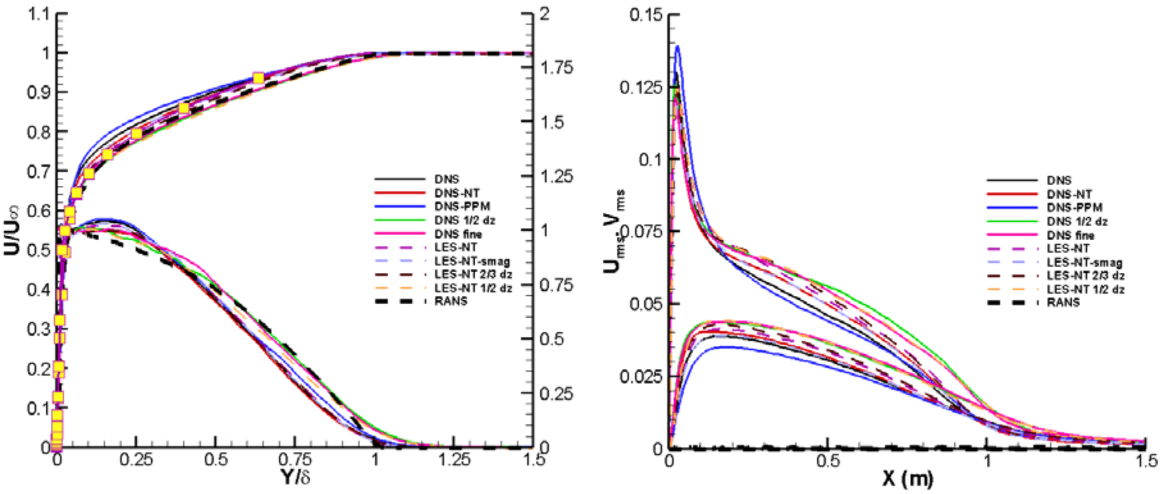

Figure 9.1.3: Axial velocity and Reynolds shear stress (right) and rms axial and normal fluctuation velocities (left) versus Y/δ

Some of the LES and DNS solutions agree better with the theoretical velocity profile than does the RANS solution. The trends exhibited by the Reynolds stress and fluctuating velocity components are as expected, though there is significant scatter among the predictions.

The primary purpose of conducting these analyses is to identify a ‘reference’ solution that can then be interrogated to determine possible weaknesses in the LES/RANS formulation and thereby focus potential improvements. It is unclear if any of the obtained solutions can yet serve as this ‘truth model’. The fact that decreasing the Z extent of the domain leads to a reduction in the boundary layer thickness complicates this assessment, as does the fact that the ‘proper’ solution of the velocity in the buffer region is not known. One way of evaluating the LES/RANS model response may be to compare forces exerted by the resolved, modeled, and molecular Reynolds stresses:

$$\left\langle \overline{F}_i \right\rangle = \int_A \left(\left\langle \tau_{ij}^{\mathrm{res}} \right\rangle + \left\langle \tau_{ij}^{\mathrm{mod}} \right\rangle + \left\langle \tau_{ij}^{\mathrm{mol}} \right\rangle \right) \cdot \vec{n}\, dA \tag{9.1.1}$$

as they vary through the boundary layer. The difference between ensemble-averaged forces from a LES and those from the LES/RANS is the form of the modeled component, which for the LES/RANS methods considered herein, includes an unsteady RANS contribution, a subgrid component, and a spatially-varying blending function that connects the two. The analogous LES method includes only the subgrid component, so for the forces exerted on the fluid for the two methods to be equal, the sum of the resolved and modeled components must balance. In general, this will not occur, and the degree of imbalance represents model form error as it is reflected in the time-averaged solution.

Based on these statistics (and similar ones associated with heat and mass transfer), it should be possible to localize potential sources for model form error. Given a particular LES/RANS model variant, it is possible to determine the ‘optimal’ model response that leads to mean-flow equivalence between the LES and LES/RANS solution on the same mesh. This response may be obtained by including the difference between ensemble-averaged forces as a source term (again with analogous expressions for the energy and species equations) that steers the ensemble averages toward those of the ‘more trusted’ LES.

$$\int_{\Omega} \frac{\partial \overline{\rho}\widetilde{u}_i}{\partial t} d\Omega + \int_{A} (\overline{\rho}\widetilde{u}_i\widetilde{u}_j + \delta_{ij}\overline{p} - \tau_{ij}^{\text{mod}} - \tau_{ij}^{\text{mol}}) \cdot \vec{n} dA = \left\langle F_i^{\text{LES}} \right\rangle - \left\langle F_i^{\text{LES/RANS}} \right\rangle \tag{9.1.2}$$

Here, $\left\langle F_i^{\text{LES}} \right\rangle$ will be determined beforehand from the wall-resolved LES and $\left\langle F_i^{\text{LES/RANS}} \right\rangle$ will be determined as the calculation proceeds by exponentially-weighted ensemble-averaging methods. The final solution for $\left\langle F_i^{\text{LES/RANS}} \right\rangle$, separated into its components, represents the ‘optimal’ force balance and thereby represents a focal point for directing model improvements. The optimal LES/RANS model will be the one that replicates the mean-flow statistics of the wall-resolved LES without requiring a forcing function.

10. Development of ‘Data-Mining’ Strategies for Analyzing Reynolds-averaged Navier-Stokes Closure Model Assumptions Based on LES/RANS data

This last part of the study investigated the possibility of ‘mining’ LES/RANS solutions to provide data that might be used to evaluate and potentially improve RANS-level models. As all two-equation and second-moment RANS models require the solution of a turbulence dissipation rate equation (in some form), the initial part of this study details the calculation of the turbulence dissipation rate ε and related turbulent flow terms by using resolved flow data from a numerical simulation utilizing a hybrid LES/RANS turbulence closure. The estimate of the dissipation rate was obtained by solving the Favre-averaged turbulent kinetic energy equation throughout the simulated flow. The constituent terms of the equation, which included fluctuating and Favre-averaged flow variables, were obtained by ensemble-averaging various resolved-scale flow data over the course of the simulation. Once the dissipation rate was obtained, it was used to estimate the specific dissipation rate, ω, and kinematic eddy viscosity, υ_t, throughout the flow. These were compared to their fully-modeled counterparts obtained using Menter’s BSL two-equation model in order to analyze the accuracy of the latter in simulating complex flows.

The flow chosen for this analysis was a Mach 2.79 air flow over a 20 degree wedge (Figure 10.1.1. The region at the start of the wedge features shock-boundary layer interaction, where the accuracy of standard two-equation turbulence models is questionable. To obtain the necessary

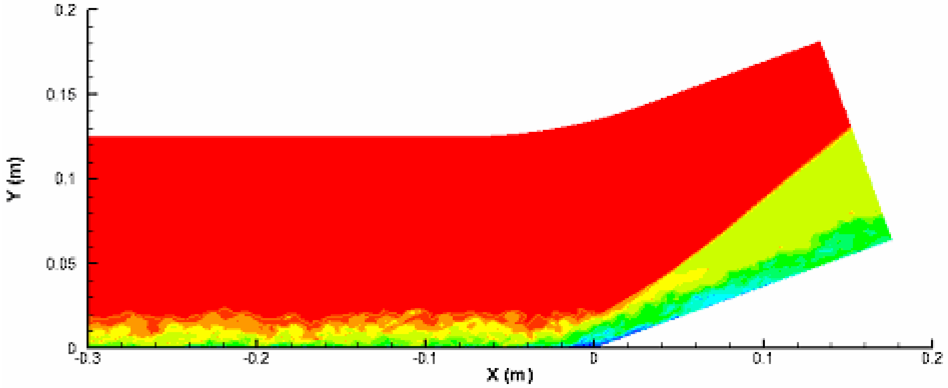

Figure 10.1.1: Instantaneous Mach number contours: Mach 2.79 flow over 20 deg. corner

time-averaged flow data, the simulation compiled averages over 13500 iterations, representing approximately five flow-through times.

The Favre-averaged TKE equation reads as follows:

$$\underbrace{\frac{\partial \bar{\rho} k}{\partial t} + \frac{\partial \rho k \tilde{u}_j}{\partial x_j}}_{convection} = \underbrace{-\tau_{ij}\frac{\partial \tilde{u}_i}{\partial x_j}}_{production} - \underbrace{\bar{\rho}\varepsilon}_{dissipation} + \frac{\partial}{\partial x_j}\left[\underbrace{\overline{t_{ij}u''_i}}_{\substack{molecular\\ diffusion}} - \underbrace{\overline{\rho u''_j \tfrac{1}{2} u''_i u''_i}}_{\substack{turbulent\\ diffusion}} - \underbrace{\overline{p' u''_j}}_{\substack{pressure\\ diffusion}}\right] - \underbrace{\overline{u''_i}\frac{\partial \bar{p}}{\partial x_i}}_{\substack{pressure\\ work}} + \underbrace{\overline{p'\frac{\partial u''_i}{\partial x_i}}}_{\substack{pressure\\ dilatation}} \qquad (10.1.1)$$

Time-averaged quantities are denoted with an overbar, Favre-averaged quantities with a tilde, and fluctuating quantities with a double prime symbol. τ_{ij} denotes Reynolds stresses while t_{ij} represents the laminar shear stress tensor. The individual fluctuation and Favre-averaged quantities were reconstructed using time-averaged data as follows:

$$\tilde{u}_j = \frac{\overline{\rho u_j}}{\bar{\rho}} \qquad (10.1.2)$$

$$\tau_{ij} = \overline{\rho u_i u_j} - \frac{\overline{\rho u_i}\,\overline{\rho u_j}}{\bar{\rho}} \qquad (10.1.3)$$

$$k = \frac{\tau_{ii}}{2\bar{\rho}} \qquad (10.1.4)$$

$$\overline{t_{ij}u''_i} = \overline{t_{ij}u_i} - \overline{t_{ij}}\tilde{u}_i \qquad (10.1.5)$$

$$\overline{\rho u''_j \tfrac{1}{2} u''_i u''_i} = \tfrac{1}{2}\overline{\rho u_j u_i u_i} - \tilde{u}_i \overline{\rho u_j u_i} - \tfrac{1}{2}\tilde{u}_j \overline{\rho u_i u_i} + \overline{\rho u_i}\tilde{u}_i \tilde{u}_j \qquad (10.1.6)$$

$$\overline{p' u''_j} = \overline{p u_j} - \bar{p}\bar{u}_j \qquad (10.1.7)$$

$$\overline{u''_i} = \bar{u}_i - \tilde{u}_i \qquad (10.1.8)$$

$$\overline{p'\frac{\partial u''_i}{\partial x_i}} = \overline{p\frac{\partial u_i}{\partial x_i}} - \bar{p}\overline{\frac{\partial u_i}{\partial x_i}} \qquad (10.1.9)$$

All quantities were span-averaged during post-processing. Gradients were then computed using a finite-volume Green's theorem formulation at each mesh cell.

For this analysis, the molecular diffusion term was ignored due to the uncertainty in estimating the shear stress tensor very close to the wall. The first term on the left-hand side was also omitted as the analysis considers a quasi-steady state solution. Finally, because the hybrid LES/RANS turbulence closure used in the simulation does not resolve turbulent eddies near the wall, it was necessary to add a modeled component to the estimate of the Reynolds stress tensor τ_{ij} when calculating the turbulent kinetic energy production rate. The modeled stresses were formed based on the Boussinesq hypothesis such that the final tensor equations were:

$$\tau_{ij} = \overline{\rho u_i u_j} - \frac{\overline{\rho u_i}\,\overline{\rho u_j}}{\bar{\rho}} - \mu_t\left(\frac{\partial \tilde{u}_i}{\partial x_j} + \frac{\partial \tilde{u}_j}{\partial x_i} - \frac{2}{3}\delta_{ij}\frac{\partial \tilde{u}_k}{\partial x_k}\right) + \frac{2}{3}\delta_{ij}\overline{\rho k_m} \qquad (10.1.10)$$

where μ_t and k_m denote the eddy viscosity and turbulent kinetic energy, respectively, obtained from Menter's BSL model.

The convection, production, diffusion, pressure work, and pressure dilatation were then evaluated as described above and used to solve for the turbulent dissipation rate. Figure 10.1.2 shows the resulting values of each calculated term in the TKE equation taken inside the boundary layer at x = -0.2 meters. The dominant term is the turbulent energy production rate, which in turn determines the dissipation rate. The remaining terms tend to be relatively small, with the exception of the region near the top of the boundary layer, where the convection and turbulent transport terms are briefly dominant. However, these two terms nearly cancel out and do not influence the calculated dissipation rate.

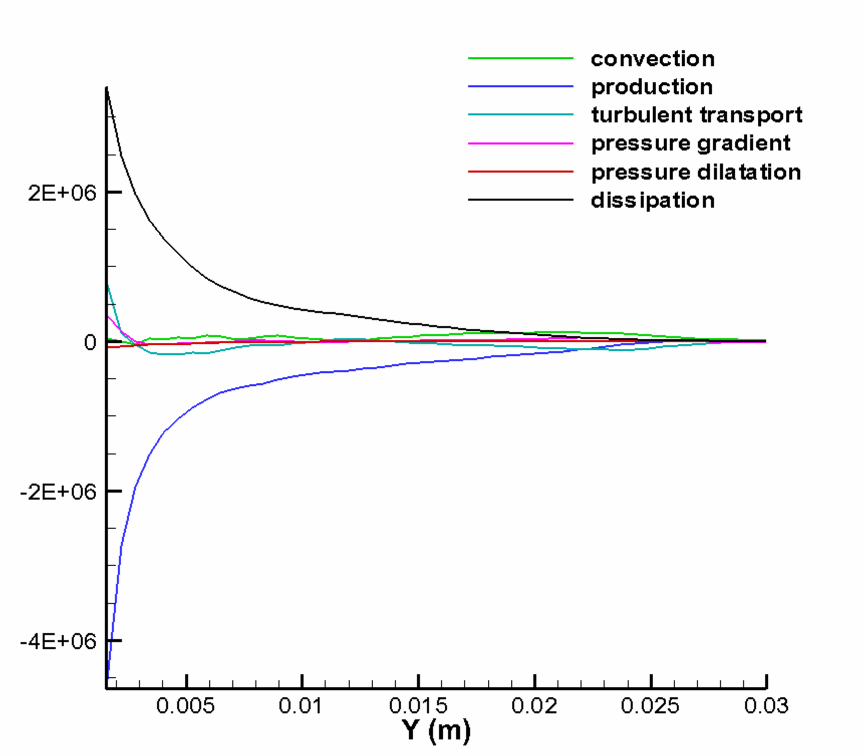

Figure 10.1.2: Turbulence energy equation balances (Mach 2.79 flat-plate boundary layer)

The specific dissipation rate and eddy viscosity were then estimated based on the turbulence dissipation rate. The specific dissipation rate was calculated as $\omega = \varepsilon / (0.09 \times (k + \overline{k_m}))$. The modeled turbulence kinetic energy k_m was added to the resolved TKE value to account for the lack of resolved eddies near the wall, similarly to the adjustment made to the resolved Reynolds stress tensor. Finally, the kinematic eddy viscosity was given by $\nu_t = (k + \overline{k_m}) / \omega$

Figures 10.1.3 through 10.1.6 show progressions of the k, ε, ω and ν_t profiles through the flow, taken along lines extending perpendicular to the solid surface. Note that for the TKE and

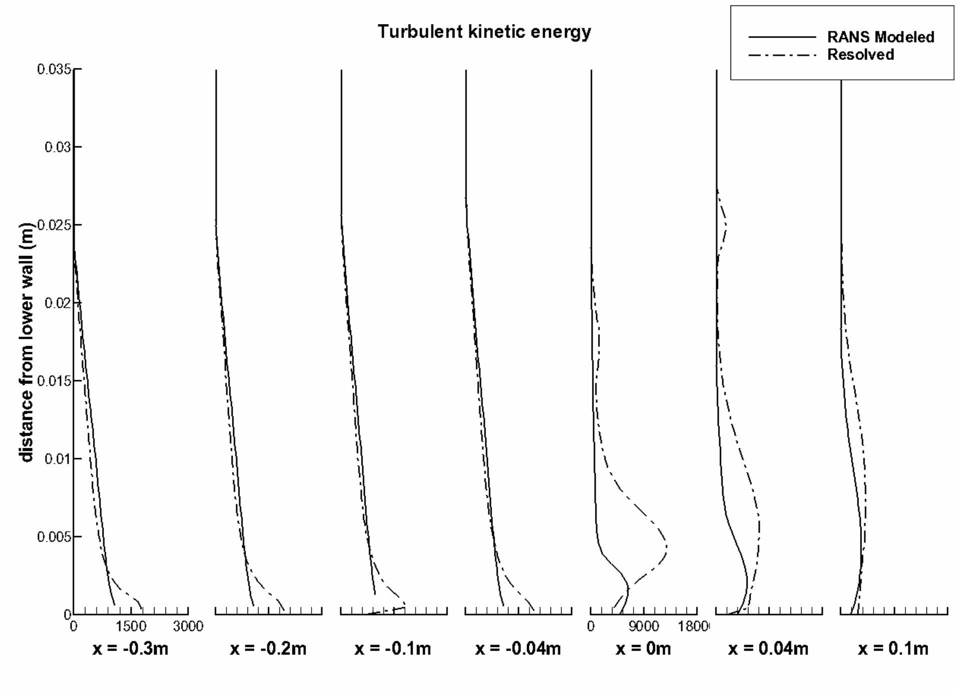

Figure 10.1.3: Turbulence kinetic energy profiles throughout interaction region

eddy viscosity plots, the scale changes after the contour at x = -0.04m, due to the increased levels of turbulence caused by the shock and recirculation zone. The resolved values based on the above analysis are compared with fully modeled versions based on a RANS simulation of the same flow utilizing Menter's BSL turbulence closure.

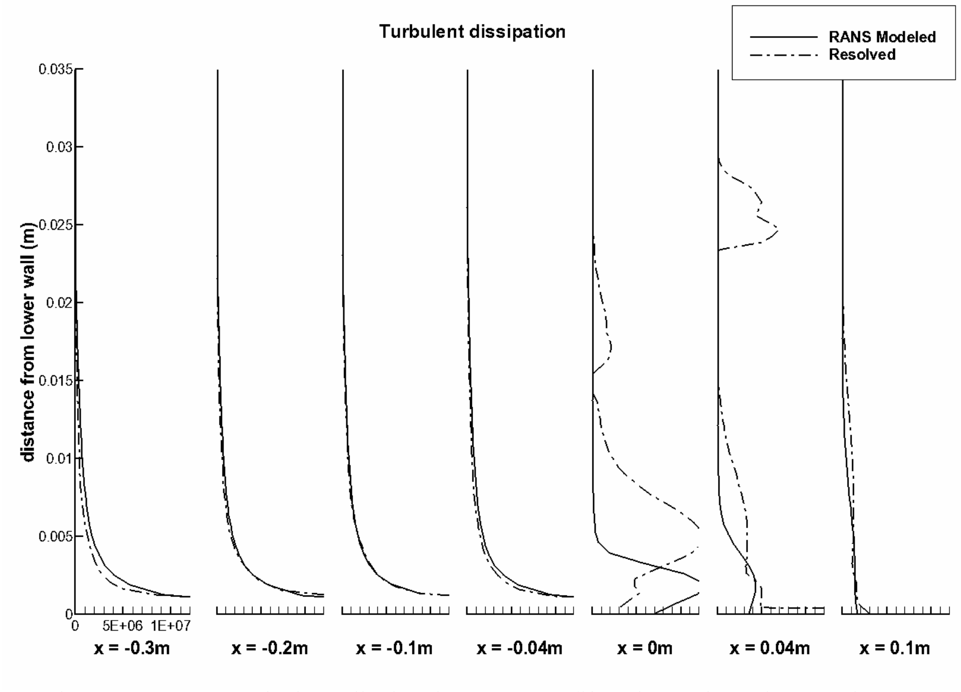

Figure 10.1.4: Turbulent dissipation rate profiles throughout interaction region

The resolved turbulent kinetic energy (Figure 10.1.3) upstream of the corner closely matches the modeled values throughout most of the boundary layer. A significant deviation occurs close to the wall, where the resolved TKE grows much larger as a consequence of being augmented by the modeled near-wall values. Past the corner, the resolved TKE significantly exceeds the model within the recirculation zone, then approaches the modeled values again as the flow re-attaches. There is also a local spike in the resolved TKE values around the shock.

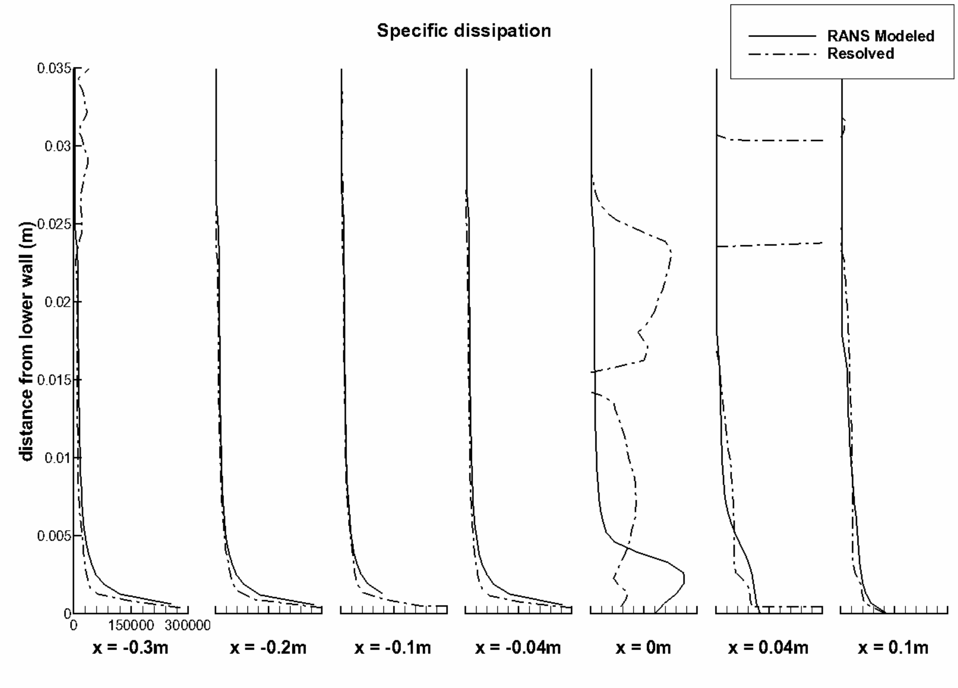

Figure 10.1.5: Specific turbulent dissipation rate profiles throughout the interaction region

The resolved turbulent dissipation rate (Figure 10.1.4) is generally in good agreement with the modeled values in the upstream part of the flow, although it is difficult to make a qualitative comparison very near the wall since both values grow asymptotically. Consistent with the turbulent kinetic energy results, the resolved dissipation rate is relatively high inside the recirculation zone near the corner, although the near-wall values at the corner itself are lower than the model predicts. The spike in the resolved dissipation rate around the shock is more pronounced due to the large contribution of the pressure work in this region.

The resolved specific turbulence dissipation rate (Figure 10.1.5) follows a very similar pattern; the main difference in the upstream region of the flow appears to be a relatively low near-wall value of the resolved specific dissipation, due to a probable over-estimate of the TKE. This effect is also evident past the corner, where the modeled specific dissipation rate is higher near the wall than the resolved. The erratic fluctuation in the resolved data beyond the top of the boundary layer in the first station is a result of dividing by very small TKE values and is not physically significant.

The resolved kinematic eddy viscosity (Figure 10.1.6) agrees with the peak modeled value in the upstream region, but is more constant throughout the entire boundary layer. The higher than

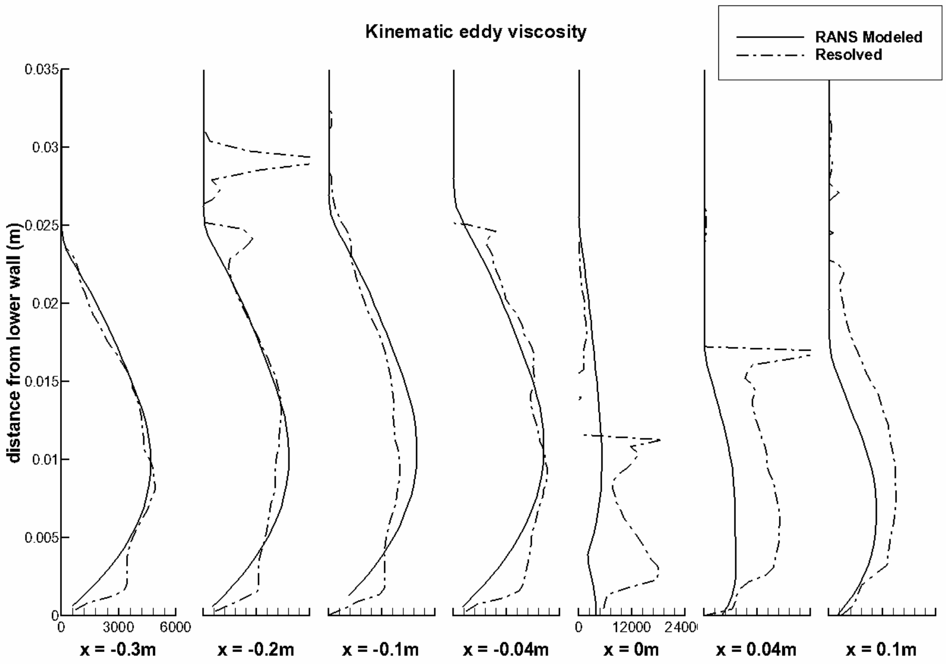

Figure 10.1.6: Kinematic eddy viscosity profiles throughout the interaction region

modeled values near the wall can be explained by the overly high resolved TKE values; however, it is unclear why the resolved eddy viscosity near the top edge of the boundary layer is significantly higher than the modeled form. Past the corner, the resolved eddy viscosity tracks the same pattern shown by the resolved TKE, with very high values in the recirculation zone. The peak eddy viscosity values occur immediately downstream of the shock, although unlike the TKE and dissipation rates, the values upstream of the shock remain consistently minimal.

These results illustrate the potential for utilizing LES/RANS data to extract turbulence information that could be used in RANS-level models. The results are sensitive to the interpretation of the RANS component within the LES/RANS framework and to the blending between the two methodologies. Future work should focus on ensuring consistency between these aspects of the model.

11. Summary

This research has developed a new hybrid large-eddy /Reynolds-averaged Navier-Stokes turbulence closure strategy specifically designed for strongly interacting, wall-bounded flows. The model differs from its predecessor in that the need to pre-calibrate a model constant is removed through the use of ensemble-averaged turbulence information to estimate an outer-layer turbulence length scale. The model has been applied to a variety of shock / boundary layer interactions and has shown a good level of predictive capability for both mean and second-moment quantities. A specific result of the shock / boundary layer interaction study is a strong correlation between the most probable time of a fluid within the recirculation region formed through shock interaction and the dominant low-frequency signal of the interaction. This provides evidence that the appearance of a low-frequency mode of separation-shock unsteadiness is intimately connected with the structure of the backflow region and the mean entrainment patterns. With this knowledge in place, it may be possible to predict low-frequency dynamics of complicated interactions by examination of the mean structure of the interactions. The LES/RANS model was also tested for turbulent flow over an airfoil near static stall as an initial step toward its use in predicting dynamic stall.

12. Other Information

12.1. Students supported and degrees received

1. Daniel Gieseking (May, 2009 – December, 2011) M.S. Thesis "A New Hybrid Large-Eddy Simulation / Reynolds Averaged Navier-Stokes Model for Compressible Flows", currently employed by Honda Aircraft.

2. Ilya A. Zilberter (January, 2012 – December, 2012) Worked on data-mining strategies using LES/RANS solutions. Currently Ph.D candidate at NCSU

3. Jianghua Ke (December, 2013 –August, 2013) Worked on airfoil simulations using LES/RANS for static and dynamic stall problems. Currently Ph.D candidate at NCSU supported by new ARO grant with Dr. Gopalarathnam as PI.

12.2. Publications directly related to this work.

Ke, J., Edwards, J.R., "RANS and LES/RANS Simulation of Airfoils under Static and Dynamic Stall" AIAA Paper 2013-0955, January, 2013

Gieseking, D. and Edwards, J.R. "Simulations of a Mach 3 Compression-Ramp Interaction using LES/RANS Models" *AIAA Journal*, Vol. 50, No. 10, 2012, pp. 2057-2068.

Gieseking, D.A. "A New Hybrid Large-Eddy Simulation / Reynolds-averaged Navier-Stokes Model for Compressible Flows", M.S. Thesis, Aerospace Engineering, NCSU, December, 2011.

Gieseking, D.A., Choi, J.-I., Edwards, J.R., and Hassan, H.A. "Compressible Flow Predictions Using Improved LES/RANS Models" *AIAA Journal*, Vol. 49, No. 10, 2011, pp. 2194-2209

Gieseking, D.A., Edwards, J.R, and Choi, J.-I. "Simulation of a Mach 3 24-Degree Compression-Ramp Interaction using LES/RANS Models" AIAA Paper 2011-5541, August, 2011.

Gieseking, D.A., Choi, J.-I., Edwards, J.R., and Hassan, H.A. "Simulation of Shock / Boundary Layer Interactions Using Improved LES/RANS Models" AIAA Paper 2010-110, January, 2010.

12.3. Technology Transfer

1. LES/RANS methodology has been implemented into NASA's VULCAN code by Dr. Robert Baurle.

2. LES/RANS methodology has been used by AFRL to simulate reactant mixing as influenced by impinging shock waves. This work was performed by Dr. John Boles of Taitech, Incorporated.
3. LES/RANS methodology has been to compute reactive flows in the University of Virginia's Scramjet Combustion Facility as part of Dr. Edwards' role as CFD lead in the National Center for Hypersonic Combined Cycle Propulsion.
4. LES/RANS methodology has been implemented into a version of Aerosoft's GASP flow solver by Reece Neal.

12.4. Other Connections

1. Daniel Gieseking defended his M.S. thesis on December 4, 2011. He is employed by Honda Aircraft.

2. Dr. Edwards and Dr. A. Gopalarathnam submitted a successful proposal to ARO that will develop new theoretical approaches for predicting forces induced during dynamic stall. Data generated from RANS and LES/RANS simulations will be used to inform the low-order theory.

3. Dr. Edwards participated in the 1st, 2nd, 3rd, 4th, and 5th Shock Wave / Boundary Layer Interaction Workshop (2009-2012), jointly organized by NASA Glenn Research Center and AFRL. Each year, some aspect of the ARO-sponsored work was presented.

4. The NCSU team participated in a blind study sponsored by AFRL in January, 2010. We computed a 3-D shock / boundary layer interaction experimentally mapped at the University of Michigan using the ARO-supported LES/RANS model enhanced by a multi-wall recycling / rescaling procedure developed using NASA support. Our predictions were in reasonably good accord with experimental measurements.

References

[1] Edwards, J.R., Choi, J-I., and Boles, J.A. "Hybrid Large-Eddy / Reynolds-Averaged Navier-Stokes Simulation of a Mach-5 Compression Corner Interaction", *AIAA Journal,* Vol. 46, No. 4, 2008, pp. 977-991.
[2] Choi, J.-I., Edwards, J.R., and Baurle, R.A. "Compressible Boundary Layer Predictions at High Reynolds Number using LES/RANS Models" AIAA Journal, Vol. 47, No. 9, 2009, pp. 2179-2193.
[3] Ghosh, S., Choi, J.-I., and Edwards, J.R. "Simulation of Shock Boundary Layer Interactions with Bleed using Immersed Boundary Methods" *Journal of Propulsion and Power*, Vol. 26, No. 2, 2010.
[4] Boles, J.A., Edwards, J.R., and Choi, J.-I. "Large-Eddy / Reynolds-Averaged Navier-Stokes Simulations of Sonic Injection into Mach 2 Crossflow". *AIAA Journal.* Vol. 48, No. 7, 2010, pp. 1444-1456.
[5] Ghosh, S., Choi, J-I., and Edwards, J.R. "Numerical Simulation of the Effects of Mesoflaps in Controlling Shock / Boundary Layer Interactions", *Journal of Propulsion and Power*, Vol. 28, No. 5, 2012, pp. 955-970

[6] Spalart, P.R., Deck, S., Shur, M.L., Squires, K.D., Strelets, M., Travin, A. "A New Version of Detached-Eddy Simulation, Resistant to Ambiguous Grid Densities," Theoretical and Computational Fluid Dynamics, Vol. 20, 2006, pp.181–195

[7] Elena, M., and Lacharme, J. P., "Experimental Study of a Supersonic Turbulent Boundary Layer using a Laser Doppler Anemometer," *Journal de Mecanique Theorique et Applique*, Vol. 7, No. 2, 1988, pp. 175-190.

[8] Luker, J. J., Bowersox, R. D. W., and Buter, T. A., "Influence of Curvature-Driven Favorable Pressure Gradient on Supersonic Turbulent Boundary Layer," *AIAA Journal*, Vol. 38, No. 8, 2000, pp. 1351-1359.

[9]Smits, A. J., and Muck, K.-C., "Experimental Study of Three Shock-Wave/Turbulent Boundary Layer Interactions," *Journal of Fluid Mechanics*, Vol. 182, Sep. 1987, pp. 291-314.

[10] Shur, M., Spalart, P.R., Strelets, M., and Travin, A.K. "A Hybrid RANS/LES Approach with Delayed DES and Wall-Modeled LES Capabilities" *International Journal of Heat and Fluid Flow,* Vol. 29, 2008, pp. 1638-1649.

[11] Donovan, J.F., Spina, E.F., and Smits, A.J. "The Structure of a Supersonic Turbulent Boundary Layer Subjected to Concave Surface Curvature" *Journal of Fluid Mechanics*, Vol. 259, 1994, pp. 1-24.

[12] Donovan, J.F. "The Structure of Supersonic Turbulent Boundary Layers Subjected to Concave Surface Curvature" Ph.D. Dissertation, Princeton University, 1989.

[13] Settles, G.S. and Dodson, L.J. "Supersonic and Hypersonic Shock / Boundary Layer Interaction Database" *AIAA Journal*, Vol. 32, No. 7, 1994, pp. 1377-1383 (see also NASA CR 177577)

[14] Dupont, P., Haddad, C., and Debieve, J.F. "Space and Time Organization in a Shock-Induced Separated Boundary Layer," *Journal of Fluid Mechanics*, Vol. 559, 2006, pp. 255-277.

[15] Babinsky, H., Li, Y., Ford, C.W.P. "Microramp Control of Supersonic Oblique Shock-Wave / Boundary Layer Interactions" *AIAA Journal* Vol. 47, No. 3, 2009, pp. 668-675.

[16] Gleyzes, C., "Operation Decrochage-Resultats des Essais a la Souffliere F2," ONERA, Technical Report RT-OA 19/5025, Chatillon, France, June, 1988.

[17] Mary, I, and Sagaut, P. "Large Eddy Simulation of Flow Around an Airfoil Near Stall" *AIAA Journal*, Vol.40, No. 6, 2002, pp. 1139-1145.